Fall 2-15-2023

Chemical Vapor Deposition Grown Monolayer Graphene Microsensors with RF Ring Oscillator Backend Circuit

Mohamed Ahmed Waheed Tawfik
mtawfik96@aucegypt.edu

The American University in Cairo
الجامعة الأمريكية بالقاهرة

Graduate Studies

Chemical Vapor Deposition Grown Monolayer Graphene Microsensors with RF Ring Oscillator Backend Circuit

A THESIS SUBMITTED BY

Mohamed Ahmed Waheed Tawfik

TO THE

MSc. Mechanical Engineering Program

29th of December 2022

in partial fulfillment of the requirements for the degree of MSc. Mechanical Engineering Program

Declaration of Authorship

I, Mohamed Ahmed Waheed Tawfik, declare that this thesis titled, "Chemical Vapor Deposition Grown Monolayer Graphene Microsensors with RF Ring Oscillator Backend Circuit" and the work presented in it are my own. I confirm that:

- This work was done wholly or mainly while in candidature for a research degree at this University.
- Where any part of this thesis has previously been submitted for a degree or any other qualification at this University or any other institution, this has been clearly stated.
- Where I have consulted the published work of others, this is always clearly attributed.
- Where I have quoted from the work of others, the source is always given. With the exception of such quotations, this thesis is entirely my own work.
- I have acknowledged all main sources of help.
- Where the thesis is based on work done by myself jointly with others, I have made clear exactly what was done by others and what I have contributed myself.

Signed:

_____

_____

Date

Abstract

This work presents the integration of a backend RF ring oscillator readout circuit to transduce structural changes in CVD-grown monolayer graphene into an electrical signal and the implementation of it to detect physical changes such as radiation and flexural strain. The novelty in this work lies in the following (1) the ability of the sensor platform to overcome environmental effects, such as light photons and temperature changes, through the readout circuit, and (2) it opens the door for the scalability of CVD-grown graphene-based for sensors and devices. Thus, the introduced sensors solve several downsides in the state-of-the-art graphene-based radiation and strain devices, such as dependency on high atomic number, fading signal problems, dependency on electron excitation to generate a signal, difficulties in fabrication of single crystals, structural instabilities due to fabrication, and toxicity of high atomic number sensing elements. In our first implementation, we introduce a new radiation detection approach by measuring the change in resistance in correlation with the incident irradiation dose. This approach solves several of the problems reported in the literature by eliminating the necessity of structural stability or fabrication imperfections, avoiding bulk volumes regarding the sensing element's geometry, and avoiding fading signal problems. Unlike traditional radiation sensors, cooling is not needed as the resolution is determined mainly by the level of structural damage, instead of the generated carriers due to incident radiation, with no toxicity problems as carbon-based materials are to be used. Sensitivity in gamma radiation detection of 7.86 kGy/Hz was measured in response to cumulative gamma radiation dose ranging from 0 to 1 kGy which is suitable in food industry applications and homeland security. Senstivity of the platform to Beta was 27 times lower than gamma due to lower energy of gamma irradiation than that of beta irradiation. The new approach helps in minimizing background environmental effects (e.g., due to light and temperature), leading to an insignificant error in the output change in frequency of the order of 0.46% when operated in light versus dark conditions. The uncertainty in readings due to background light was calculated to be in the order of 1.34 Ω, which confirms the high stability and selectivity of the proposed sensor under different background effects. Our second implementation used the same platform on a flexible substrate as a new approach to detect flexural strain. This was achieved by dependency on the structure deformation method to overcome the limitations of the other mechanisms, such as low flexural strain sensitivity and lower gauge factors at low strain levels. Unlike traditional metal-foil strain sensors, the simple fabrication avoids structural damage in the monolayer graphene sheet. The sensor platform is also marked by having high flexibility and high conductivity combined with a high signal-to-noise ratio, with no need for calibration merged with high flexural sensitivity as monolayer graphene hinders creation of conductivity channels through straining. Our flexural strain sensor has a gauge factor of 64.36, corresponding to a change in frequency of 7.42%, achieving a sensitivity of around three times higher than sensors in literature working in the same strain range.

Acknowledgements

I would first like to thank my thesis advisor and mentor Dr. Mohamed Serry. The door to Dr. Serry's office was always open whenever I ran into any problem throughout my research or even my career. I appreciate his guidance and efforts that built a respective researcher and teacher, willing to contribute in the academic career. His investment in me changed me to a better person I wished to be one day. I would like also to thank Dr. Abdelhameed Sharaf for his valuable contribution in this research and his great experience, that brought this work to light.

Finally, I must express my very profound gratitude to my parents for their unconditional love and support and to my friends for backing me up and for their encouragement throughout my years of study together with the process of researching and writing this thesis. This accomplishment would not have been possible without them.

Thanks,

Contents

List of Figures

List of Tables

List of Abbreviations

REO	**Rare Earth Oxide**
Co-60	**Cobalt-60 isotope**
MOS	**Metal oxide semiconductor**
MA	**Methyl ammonium**
FA	**Formamidinium**
FET	**Field effect transistor**
GF	**Gauge factor**
%vol	**Percent volume**
PDMS	**Polydimethylsiloxane**
wt%	**Weight percent**
S/N	**Signal to noise ratio**

List of Symbols

N	*number of inverter stages*
Ron	*Resistance between gate and source in on mode*
Cd	*Drain capacitance*
Cg	*Gate capacitance*
M	*number of graphene sensors*
Rg	*Original resistance of graphene*
ΔRg	*Change in Graphene resistance*
$\frac{\Delta F}{F}$	*Normalized change in frequency*
F_{osc}	*Oscillating frequency*
F_g	*running frequency due to graphene*
k	*ratio between gate and drain capacitance*
γ	*complex constant*
$w_{\frac{\Delta F}{F}}$	*uncertainty in measuring frequency*
$W_{\Delta Rg}$	*uncertainty in calculating change in resistance*
N_D	*Defects density in graphene*
λ_L	*Wavelength of laser used in Raman spectroscopy*

Chapter 1

Introduction

1.1 Graphene

By definition, Graphene is a two-dimensional material of one atom thick, consisting of carbon based structure packed densely using sp2 bonds in a repetitive hexagonal pattern. It can also be described as a single perfect layer of graphite. Two dimensional materials especially graphene are highly emerging as promising candidates for micro devices and sensors, due to their distinctive electronic and mechanical properties. Graphene's high potential to be used in sensors and micro devices emerges from the fact that each atom is solely exposed to the external environment or subjected change of any type and directly interacts, changing the structural properties of graphene and thus the electronic properties of the material[1].

Graphene possess distinctive mechanical properties along with exceptional electronic properties of being a zero gap semiconductor allowing easier excitation of electrons than any other material, which in return gives graphene piezo resistive behavior. Piezo resistive materials are ones that interacts in the form of a change in electronic or electrical properties when subjected to a mechanical strain. Mechanical properties of graphene were measured accurately in literature and was also assessed computationally for validation, and it was found that the young's modulus, tensile strength and second order elastic stiffness are of 0.5 TPa, 130 GPa, and 340 Nm^{-1} respectively. Combined with those exceptional mechanical properties are exceptional electronic properties, of having conical valence and conduction bands that touch in a single point called Dirac point at the high symmetry K and K' points of Brilluoin zone. These properties allow electrons to have a quasi-relativistic behavior which has to be characterized using Dirac equation[2]. All of these properties nominates graphene to be utilized as a sensing element in multiple sensors, most importantly radiation sensors and strain sensors.

1.2 Radiation Interaction with Graphene

Radiation can be classified into two main types: particle radiations such as alpha, beta, neutrons, protons, and electromagnetic radiation which includes the electromagnetic spectrum

but most commonly X-ray and gamma radiation. Alpha and Beta radiation can cover shorter distances than electromagnetic radiation in any material, and can be stopped easily using a sheet of paper. Beta radiation is the result of radioactive excitation that happens in the nucleus, which can be in one of two forms, either negatively charged electrons which is called beta minus, or positively charged positron and called beta plus. Beta radiation, can travel longer distances in air, but can be stopped easily in the body with a penetrative distance of 3.8 cm, in these means Beta radiation can cause skin cancer due to being an ionizing radiation that will invade the body till stopped by skin[3].

Gamma radiation is a photonic electromagnetic radiation emitted after relaxation of daughter nucleus through radioactive decay of the original or parent nucleus. Gamma radiation can cover a larger distance in any matter than any other type of radiation, due to its high energy so it can penetrate the human body in high depths. High doses of Gamma irradiation can cause some serious health problems, due to its ionizing nature. It can eliminate electron form a matter which can interact with a neighbor nuclear causing a positron emission in an indirect ionization process. This interaction can easily damage DNA, causing a range of different cancers, for example bone, breast, skin, bone, and leukemia[4].

Gamma radiation interacts with any material in one of 4 different ways as shown in Figure 1. Coherent scattering is the first way of interaction between gamma radiation and a matter or material, where part of the incident energy of the radiation is passed to an electron. This amount of transferred energy is mainly dependent on scattering angle and backscattering energy. Photoelectric absorption is the second way of interaction, where the incident energy is fully absorbed by the electron causing ejection of an electron, and then series of secondary ionization processes occur. Compton scattering is the third way and is most commonly happening when gamma ray energies are moderate or in the range of 300 keV. In this inelastic scattering process, scattered gamma rays are of lower energy and higher wavelength than the incident ones, causing excitation of electron or a charged particle which then recoils conserving the energy of the whole system. Finally, pair production is the process that occurs at high gamma radiation energies of higher than 1.022 MeV, so as energy of gamma irradiation increases, the probability of having a pair production increases[5].

Radiation is used in multiple disciplines and technologies such as in industrial quality monitoring, nuclear detections, Pharmaceutical applications, border security, medical diagnosis and validations, and astrophysics[6,7]. Due to environmental concerns nuclear energy is now well established and is highly used due to its low carbon emissions with minimal wastes that might cause a negative impact to the environment. Nuclear energy is well correlated with radiation, which as mentioned before can easily interact with surrounding materials affecting human health and environmental ecosystems[5]. Radiation continuous monitoring is highly needed in all of these applications and technologies, which has to be set with the scientific health

boundaries to protect the working manpower and surrounding ecosystems from the consequences of high doses.

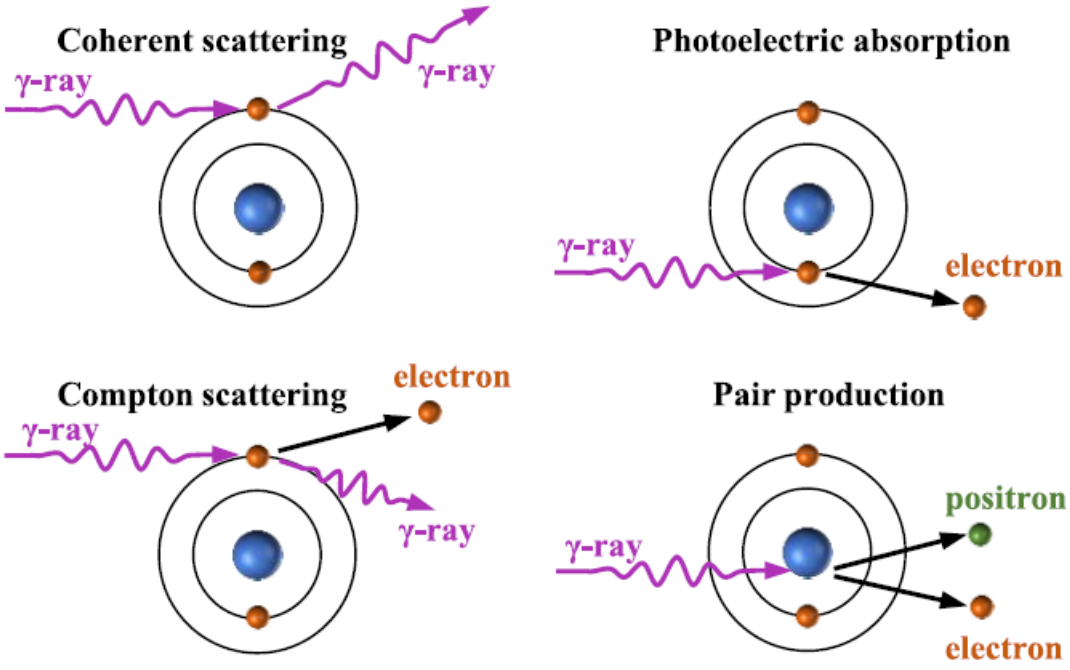

Figure 1: Illustrative diagram showing how gamma rays interacts with matter[5].

1.3 Radiation Sensors and Their Properties

Modern Gamma ray detectors are classified according to their mechanism of converting incident ray to a physical change. There are two main types of detectors: indirect conversion detectors and direct conversion detectors. Indirect conversion detectors are mainly optical detectors or scintillators, where electron hole pairs caused by incident radiation are converted to lower scale energy photons in an indirect way and finally to an electronic signal. On the other hand, direct conversion detectors or solid state detectors mainly generates direct electronic signal when the detector is subjected to radiation and electron hole pair is created, which cause accumulated charge, thus and electronic signal is formed[5].

Solid state detectors are known for being portable, cost efficient when it comes to fabrication, have higher sensitivity, and high energy resolution relative to scintillators. On the other hand, conventional or gas-filled detectors and scintillators have several limitations such as being easily affected by humidity and barometric pressures[8], also have slower response, and lower selectivity due to the fact of being easily affected with background effects such as light, as long as lower response with higher radiation energies[9,10]. Ergonomically speaking, gas-filled detectors and scintillators are large, heavy, bulky, and can't be worn or be utilized as being

wearable, and also attributed to high power consumption[11].

Sensing materials in gamma radiation solid state detectors are chosen based on some needed requirements, such as having high atomic number or Z to increase cross section of Gamma ray, having the ability of generating higher carrier density relative to the incident radiation, shouldn't contain radiative isotopes to avoid any interference with the main source. Another requirement is to have the ability for long term operation, without complete change in structure that affects the whole detection criteria, or in other words controllable change that is selectively affected by the radiation in controlled way. Low defect density is also needed, as long as being resistive to dark current, and having high carrier mobility lifetime, which is the time needed by the generated carriers to recombine after being created[12,13].

1.4 Sensing Materials in Solid State Radiation Detectors

As mentioned in the previous subsection, there are some requirements or properties that should be available in any solid state radiation detector. Research teams worked so hard to achieve those requirements by selecting and engineering wide range of sensing materials that balances between the needed properties, cost, and being easily tailored as wearable sensors to ease its usage.

1.4.1 Rare Earth Oxides (REOs)

There are general advantages when it comes to rare earth oxides as sensing elements or materials in solid state radiation detectors. REOs are easy to be doped in any material, and that could reduce the cost of using bulk rare earth oxides as sensing elements, but use a semiconductor doped with the sensing material. They are also high temperature resistant, so in industrial conditions that requires radiation detection such as steel industry, rare earth oxides can be a good sensing element candidate[14].

Samarium Oxide, Sm_2O_3 is the first REO to be utilized as solid state radiation sensor to be employed in MOS device. It was mainly designed and used as it's affected as a material by frequency dependent radiation, where frequency dependent charges are induced in the system affecting the electronic properties of the material itself, thus a direct signal[15]. Er_2O_3 was also used but under a zero gate bias between its nodes, which shows a better performance as a sensing element than Sm_2O_3, due to its higher band gap which allows Erbium oxide, Er_2O_3 to resist induced carriers by excitation due to light or higher temperatures[16].

Gadolinium oxide, Gd_2O_3 on the other hand, was used as a sensing element by deposition over p-type silicon substrate by RF sputtering. The sensing element showed a lower

performance when it comes to sensitivity to different ionizing radiations in comparison with Sm_2O_3 [17]. Ytterbium oxide, Yb_2O_3 was also utilized in a MOS based radiation sensor, the sensitivity was considered higher than most of the REOs candidates, but a fading signal problem evolved under zero gate bias when used with Co-60 source for gamma radiation detection. It also showed a steady performance with wider sensitivity domain as a field effect transistor than Gd_2O_3 and Er_2O_3 [18] .

1.4.2 Halide Perovskites

Before Perovskites, Germanium was used in radiation detection as sensing element as it generates carriers when subjected to radiation, due to its superior semi conductive properties. Germanium can also be fabricated easily as a single crystal with minimal level of defects density. Those superior semi conductive properties lead to a problem which is the easiness of electrons excitations at higher temperatures and light, so the fabricated sensors must be implemented in liquid nitrogen temperatures to overcome this problem, and also its low mass number or Z limits its fabrication volume to be high, in order to be able to stop the radiation completely[19].

Halide perovskites were introduced to overcome semi conductive problems of germanium and REOs and the fading problems of REOs. $CdTe$, CZT, and $TlBr$ were studied due to their high Z numbers that easily stops hard radiation, so lower volumes are needed to build an effective sensing element. Those advantages were accompanied by some problems such as difficulties in growing single crystals that have low defects density, which causes some problems in electron hole mobility[20]. Lead halide perovskites showed record breaking performance and sensitivity when it comes to ionizing radiation detection due to its high Z number, but it showed a severe problem of ion migration, which causes instability issues and inaccurate readings of incident ionizing radiation [21-31]. Ion migration in organic-inorganic perovskites is considered as intrinsic property that occurs upon fabrication, which causes multiple problems such reading fluctuations in the form of hysteresis, phase segregation, interfering polarization which in return can cause deterioration in carrier transport properties. It also needs to be fabricated in the form of high thickness single crystals due to the induced defects upon fabrication. Lead halide perovskites can also cause toxicity and health problems in prolonged exposures [32–38].

$FAPbT_3$ is considered one of the organic-inorganic 3D perovskites, which are designed specifically to enhance the toxicity and low band gap problems. However, $FAPbT_3$ has another problem of phase transformation after a maximum period of 1 week due to its low structural stability. Phase transformation weakens the performance of radiation detection by time, so adding Cesium cations and bromide anions enhances the phase instability problem to a working period of 4 months but doesn't eliminate it, and those additions was found to prolong carrier lifetime [29]. On the other hand, MA based organic-inorganic perovskites were studied for their much higher phase stability than that of FA based perovskites. MA based perovskites shows

better sensitivity and general performance in detection gamma radiation than FA based perovskites, especially when doped with chloride anions [39–41].

When it comes to contact or nodes for radiation sensors and micro devices, Schottky type or unbalanced contacts are favored for dark current resistance, to enhance energy resolution. MA based perovskite radiation sensors were studied with Schottky type contacts, which were deposited over the sensing element in the form of Gold and Gallium. After characterization of the sensor it was found that mild cooling is needed to improve resolution, accompanied with ion migration occuring due to induced voltage between the nodes leading to a drop in resolution [27]. Further enhancements were introduced in the form of 2D organic-inorganic perovskites, where it shows higher stability than bulk or 3D perovskites, when it comes to phase stability over time, due to the presence of organic layers or spacers. 2D perovskites showed distinguished sensitivity in sensing X-rays [42–45].

Hybridization between MA based perovskite and 2D perovskites was furtherly used by coating a layer of 2D perovskite over $MAPbI_3$. This approach showed a significant increase in energy resolution[46], so thermal stability is the key problem when it comes to the phase stability of organic-inorganic perovskites. Inorganic perovskites such as $CsPbBr_3$ and $CsPbCl_3$ showed better reliability in phase stability due to the absence of the organic element [47]. $CsPbBr_3$ showed easiness in fabrication of crackless single crystals with high purity, which leads to better performance than any of the organic-inorganic perovskites, by being highly linear and durable. Schottky or asymmetric connectors were applied to allow the sensor to withstand high electric fields while possessing low dark current [28]. High crystal quality of $CsPbBr_3$ makes generation of carriers with higher lifetime possible, in parallel with increasing energy resolution, and excellent thermal stability [30]. As mentioned before one of the main problems when using lead containing materials is the possibility of having serious health problems due to its high toxicity[48], so in literature Lead was better replaced with another atoms such as Sn, Ge, Bi, and Cu, to avoid this issue [49,50]. $Cs_3Bi_2I_9$, $Cs_3Sb_2I_9$, and $Rb_3Sb_2I_9$ showed response to alpha particles, especially ^{241}Am, but no response for Gamma radiation due to its low carrier generation caused by radiation [35].

1.4.3 Graphene and Graphene nanocomposites

Graphene is an excellent candidate for high energy radiation detection, especially photonic radiation such as: gamma and X-rays, due to its high sensitivity to local changes in its electric fields generated from the incident radiation. Electric field changes are measured using FET devices that is lately utilized with graphene. The measuring criteria of radiation is mainly based on the change in Dirac voltage caused by radiation induced charges or carriers. As mentioned before, Gamma irradiation allows for Compton scattering, where an electron and positive ions are ejected from the material upon being subjected to gamma radiation. These

ejected electrons can interact with neighbor atoms ionizing it, forming induced vacancies and interstitials due to oxidation in air and p-doping with hydroxyl, or carboxyl functional groups, which then affects the Dirac voltage of the induced electric field in the FET sensor device[51].

Jain et al. fabricated graphene based field-effect transistor which was used as a radiation dosimeter. Throughout the study they discussed the effect of radiation on some electronic properties such as Dirac voltage, and p-doping, which affects the mobility of electrons. Monolayer Graphene was transferred over a substrate of a back gate forming the needed structure of graphene based field effect transistors. This structure was irradiated with a Co-60 source with a range of doses ranging between 1 KGy to 20 KGy which is considered as medium to high dosage showing a sensitivity of approximately 1 V/KGy. This sensitivity is evolved from the Dirac point shift and the electron-hole mobility, which affects the gap properties of the material. One of the uncovered parts in the literature is the characterization of the sensor in lower doses which is highly important in biomedical and pharmaceutical industries [52].

Similarly, Patil et al worked on integrating monolayer graphene as a radiation sensing material. They used the same graphene based field effect transistor concept as Jain et al., and studied the effect of ionizing radiation on the graphene electrical properties. It was reported that local changes in electrical field due to radiation affects electrical properties ending with a signal generation using gate voltage between graphene and the back absorber used in the fabricated sensor. Their sensor was fabricated using three layers: graphene layer deposited over an insulation layer, and all are bounded to Silicon layer for radiation absorption or stopping. X-rays, gamma rays, and light photons were used to irradiate the sensor, where a 70% change in the material's resistance was captured as a signal in the case of X-rays at room temperature. The technology used in this sensor showed slow response due to carriers' accumulated charges and low carrier lifetime. It was also observed that selectivity of the sensor to the background light photons is minimal, so it has to operate under low light intensities to disallow any interference with the targeted signals [53].

Another effort in tailoring the use of graphene in wearable radiation sensors were made by Feizei et al. Reduced graphene oxide nano flakes in PMMA were fabricated to measure dose rate of gamma radiation, where graphene oxide flakes were dispersed in the polymer matrix as long as two silver coated glass parts acting as electrodes. Linear Sensitivity was recorded in a low range of dose rates which is around 50-130 mGy, with a complete absence in the higher dose rate. This can be attributed to the highly induced defects density in graphene oxide, which can easily affect the carrier mobility of electrons, and lower the performance of the sensor as a conductive cell. Also partial reduction of graphene oxide affects directly the conductivity of the sensing material itself, leading to lower electric field and thus less sensitivity [54].

1.5 Graphene based Strain Sensors and their properties

Piezo resistive property is a behavior observed in materials, when a change in electrical properties such as: resistivity, band structure occurs as a result of any applied strain using any form of stress. History behind piezo resistive property starts back in 1856, when Thomson first stated that resistance of copper is reported to be changing upon elongation [55]. After these findings, researches started flowing in the field of strain detection using piezo resistive materials to reach the highest gauge factors, so piezo resistivity is a property needed in material selection of a strain sensor to achieve the needed electrical signals. Gauge factor (GF) can be defined as the ratio between the relative change in electrical property and applied strain [56]. Flexible and wearable sensors are highly used recently in multiple fields such as robotics, healthcare, electronics and communications, so flexibility is needed in materials selection for sensing elements of strain sensors [57].

Metals and ceramics show a good potential as sensing elements, but their intrinsic brittleness and hardness lowers any utilizing possibility in flexible sensors [58]. Nanomaterials have been studied lately for their outstanding properties such as: high flexibility, low cost, and light weight. Through those lines, recent researches reports graphene to contain all of the needed properties in any strain sensor [59]. Graphene also possesses indirect proportionality between its strain sensitivity and thickness, which can be attributed directly to the weak Van der Walls bonds between layers in bulkier carbon structures or high dimensional structures, so structurally speaking, graphene can be considered highly sensitive due to its layer atomic thickness [60].

Utilizing graphene in strain sensors is based on multiple detection methods, which are all in use of piezo resistive behavior of graphene. Those methods are: multiple graphene sheets over connection, tunneling effect among neighboring sheets, and finally structure deformation. In over connected graphene sheets, larger sheet of multilayered graphene can be considered as a network of connected monolayer graphene domains or flakes. Applying any strain on the interconnected structure can easily affect the contact strength of neighboring domains, decreasing the contact surface area which affects the overlapping between the domains, and thus the electrical and electronic properties of the sensing element as illustrated in Figure 2 [56–61].

Tunneling effect among neighboring graphene sheets is considered as one of the mostly used detection methods that graphene based strain sensors are based on. It's is mainly implemented by fabrication of nanocomposites that usually consists of a polymeric matrix and graphene sheets with concentrations lower than that needed in over connected graphene sheets method. Electrons tend to tunnel through the distance between two graphene sheets, overcoming the

high potential barrier caused by the polymeric matrix. Literature reported that this mechanism is highly dependent on the distance between graphene domains. When strain is applied, distances between graphene domains increases and resistance increases drastically as shown in Figure 2. This method is highly dependent also on the homogeneity of the domains dispersion, which may affect the repeatability of the fabrication process. On the other hand, this method is reported to have the highest average of gauge factors among all of the mentioned methods [62].

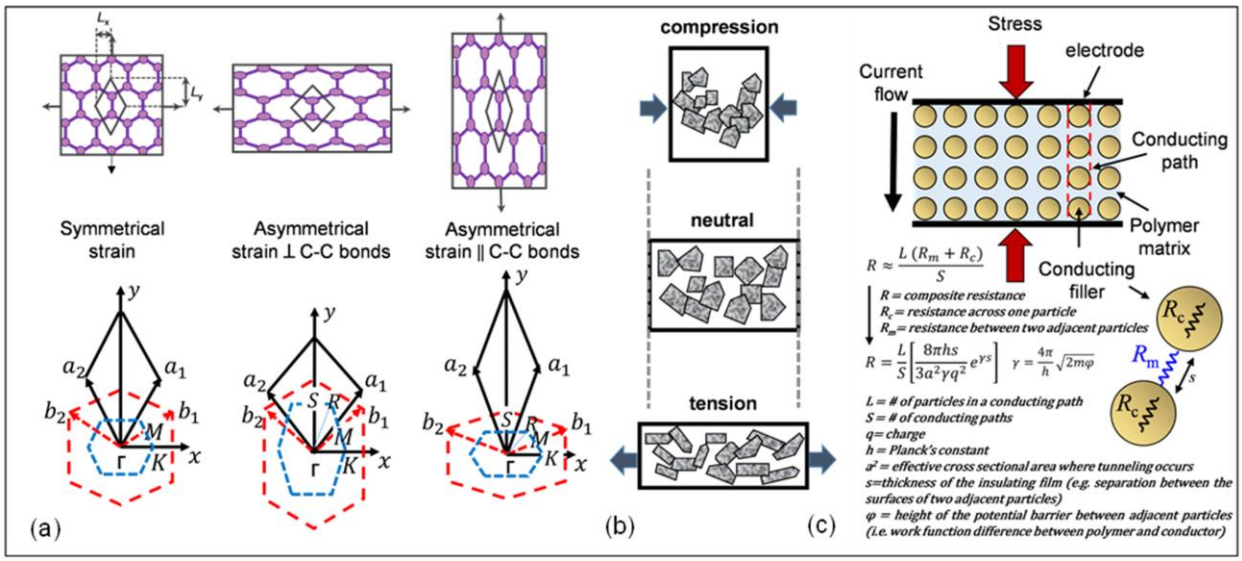

Figure 2: Diagram showing different mechanisms of strain sensing using graphene[63].

Structure deformation uses the electromechanical coupling in graphene, which is directly related to the hexagonal structure of graphene itself. Straining of the graphene domain, affects the structural orientation of covalent bonds leading to a change in band structure and electrical properties, which varies according to directionality of the applied strain [64-68]. Asymmetrical applied strain results in opening of the band gap at Fermi level by opening the Dirac point and allowing a change in electrical properties as bang gap increases proportionally with the applied strain amount [69].

1.6 Sensing Materials and Mechanisms in Strain Sensors

Previously mentioned nanocomposites using graphene sheets and polymeric matrices are the most commonly used sensing elements in literature. Anas et al. [70] worked on fabrication of graphene nanoparticles dispersed in polystyrene. The fabrication process can be described as straightforward and easy, in comparison with the known fabrication techniques. On the other hand, their sensor was accompanied with traditional gauge factor range of around 4.6. Polystyrene exhibits all of the needed flexibility in the strain sensor. Lu et al. [71] worked on enhancing dispersion of graphene nanoparticle in epoxy matrix, by using ultrasonic and ball mill processes. The suggested fabrication technique can easily affect the quality and morphology of

the produced graphene and affect its sensitivity to straining which was reflected in their sensor's gauge factor. Traditional range of gauge factor is reached ranging between 6.5 in low strains of 0-0.5% and 11.6 in higher strain levels of 0.5-1.67%.

Lu et al. [72] worked on enhancing the fabrication process of the graphene nanoparticles in epoxy matrix again by coating the nanocomposite on glass epoxy fabricated prepregs, to minimize the high level damage of graphene caused by the previously mentioned fabrication process by them. Sensor is distinguished with a low level of %vol graphene nanoparticles needed for percolation, but still has the same problem of low gauge factor which ranges between 11.81 in higher strain levels of 0.6-1.2% and 22.45 in lower strain levels of 0-0.2%.

Montazerian et al. [73] worked on an optimized and tunable fabrication process, where graphene nanoparticles concentration can be varied in the used solution for easier percolation control. Dip coating of graphene solution over spx yarn was used to deposit graphene nanoparticles, followed by dehydration. Fabrication process is repeated till the needed morphological and electrical characteristics are reached. Sensor is then added into a silicon rubber to protect it and increase its durability. Low gauge factors of less than 20 were observed at strain levels lower than 0.4% which can be attributed to the low percolation %vol used in the process.

Moriche et al. [74]worked on fabricating highly dispersed graphene nanoparticles in epoxy matrix by probe sonication. They reported that low sensitivity is observed in flexural straining, as it creates new conductivity channels, which highly affects the sensitivity of the sensor. Gauge factors in low levels of strains ranging between 0.5 and 2.5 doesn't exceed 36 which proves that tunneling effect among neighboring graphene sheets mechanism doesn't suit flexural strain sensing. On the other hand, Liu.et al [75], fabricated interconnected graphene tube sensor using graphene woven fabric and PDMS matrix. The reported sensor showed higher performance in tensile strain than flexural strain, reflected as an average of gauge factor under tensile strain and flexural strain of 219 and 70 respectively. Fiber orientation of Over connected graphene sheets highly affects sensibility towards bending strains, but still higher in performance than Tunneling effect among neighboring graphene sheets when it comes to bending or flexural strains.

Similar to our sensing material, Mahmoud et al. worked on fabrication of uniaxial aligned monolayer graphene sheets in polysilicon nanocomposites using a powder roll mixing followed by hot pressing. Their sensor showed average gauge factor upon tensile strain that ranges between 6.9 to 76.8 through different wt% of added graphene to the polysilicon matrix. The Sensor also showed an electron tunneling interaction through tensile straining causing exponential change in resistance when strained due to the increase of distance between monolayer graphene tubes. Flexibility and maximum strain are shown to be low for the fabricated ceramic composite which can highly affect sensitivity at higher strains than 7%[76].

All of the mentioned literature are mainly dependable on one of two sensing methods, either tunneling effect among neighboring graphene sheets or over connected graphene sheets, with minor dependency on structure deformation method.

1.7 Intrinsic Problems of Radiation and Strain Sensors

Radiation detection through solid state detectors in literature are mainly dependent on the current induced by separated charge carriers due to interaction with incident radiation. This concept constrains material selection and device design to some properties that has to be in any solid state sensor sensing material or device such as having high atomic number, generating higher carrier densities, avoid interference with the main source by not using radioactive isotopes, lower defect densities for better carrier mobility, resistivity to dark current by choosing better connection nodes, and to be resistant to dark current. Those constraints lead to performance affecting problems that were mentioned in literature such as fading signal problems, high level cooling with some sensing materials, bulk volumes are needed with lower atomic number elements, difficulties to grow single crystals for better carrier mobility, structural instabilities leading to performance issues, and the high toxicity of some of the used elements.

On the other hand, utilizing graphene in strain sensing also faces some problems in literature. All of the reported problems were directly related to the sensing mechanism and fabrication process. Tunneling effect among neighboring graphene sheets faces multiple problems such as being highly dependent on dispersion of graphene, and all of the reported fabrication techniques tend to use fabrication and dispersion methods that tends to make structural damages in graphene domains such as ball-milling and sonication, which in return affects sensor's performance. Lower sensitivity in lower strain range is another problem, which is highly related to the small change in distance between domains, that is not enough to produce a tangible change in electrical properties, and thus a small gauge factor. In the same manner, flexural strain tends to create conductivity channels, showing the disability to produce high gauge factor when sensing this type of strain. Through tunneling effect mechanism.

1.8 Proposed Solutions for Intrinsic Sensors Problems

In our work, we are proposing a new criteria of radiation detection, in which the change in resistivity of the graphene due to the structural damage caused by incident radiation is the main measurement needed. This permanent change is formed from the previously mentioned effect of Compton scattering, but in our case we are not measuring the change in Dirac voltage or electric field changes due to the induced defects, but measuring the change in resistivity of

the graphene, which is affected by incident radiation due to p-doping and induced defects. This approach saves most of the mentioned problems in literature as it embraces the fabricated sensor from the properties constraints, so no structural problem or fabrication difficulties are to be faced, with no need for bulk volumes when it comes to the sensing element's geometry. Mild cooling isn't needed as resolution is determined by the level of structural damage not the generated carriers due to incident radiation, with no toxicity problems as carbon based materials are to be used.

Besides, in this work, for the first time, we report a strain sensor based on the integration of monolayer CVD grown graphene on Cu-foil with an RF ring-oscillator backend platform. The proposed platform features high dependency on structure deformation detection method to overcome the limitations of other mechanisms regarding low flexural strain sensitivity and lower gauge factors accompanied with low strain levels. Simple fabrication process also avoids any possibility of any structural damages of the monolayer graphene sheet. The sensor is also marked by having high flexibility and high conductivity combined with high signal-to-noise ratio on a digital sensing platform.

Chapter 2

Transducer RF Ring Oscillator Circuit

2.1 Types of Radiofrequency oscillators

There are multiple different types of radiofrequency (RF) oscillator circuits, all of which transform change in resistance or capacitance into frequency signal [77]. LC tank oscillators [78], crystal oscillators[79], and ring oscillators are the most commonly used types of oscillator circuits as sensors transducers [80-82]. Although LC tank oscillators are highly used in multiple fields such as high frequency heating and RF generators, due to their low power consumption and simple design, they are rarely used in sensors technologies due to their high phase noise caused by switching pair and tail transistors, requiring filters to remove the noise and allow for better S/N ratios [83].

Crystal oscillators have high frequency stability accompanied with high quality or Q factor and better performance under elevated temperatures than any other type of oscillators, as long as good phase noise performance. They are mainly used in multiple applications which are mainly dependent on clock signals such as clocks radios and computers [84]. However, crystal oscillators are highly accompanied with delay in output circuit signal, and high supply voltage [85], which limits its used in sensors technologies as a transducer generating an output or readout signal. All of the mentioned oscillators circuit are highly affected by jitter and parasitic effects and less controlled oscillation amplitudes. Crystal oscillators are mainly chosen for its signal stability, but its low range of frequencies isn't tunable in this specific application of radiation and strain sensors, as wide range of doses are to be tested, stretching the needed range of frequency by the transducer, so ring oscillator circuit were a better choice due to its wider range of frequencies and its high sensitivity to changes in resistances [86]. Ring oscillator circuits are also known for its low power consumption and its high ability to inhibit and solve jitter problem caused by the used components or any source.

Dai et al. worked on integrating humidity sensor with backend ring oscillator circuit with three stages of inverters all are connected to the fabricated capacitive sensor. The aim of the used ring oscillator circuit is to form a voltage feedback loop, and as the humidity interacts with the sensor varying its capacitance, oscillating frequency of the ring oscillator varies, converting humidity sensor capacitance to a readable signal of changing frequency [87]. In another research Dai et al. worked again on integrating the same ring oscillator concept in a pressure sensor, where a capacitive pressure sensor consisting of 16 parallel pressure cells are connected to ring oscillator circuit, to convert applied pressure into change in frequency signal, which in return

showed linear performance till 500 kPa of applied pressure [88].

2.2 Design and Mathematical Modelling

Transducer design or backend readout circuit was mainly designed for multiple reasons: inhibit noise by increasing S/N ratio, enhance signal quality by removing any induced jitter, and to increase the selectivity of the sensor to irradiation and strain over ambient light or background environmental conditions, which may affect the sensor reliability. The main aim of the circuit is to transform any change in resistance to an amplified readable frequency signal.

Our RF ring oscillator transducer readout circuit is designed to be a five stage ring oscillator with two series connected graphene sensors after stage one, and after stage 3. The ring oscillator circuit consists of 4 identical inverters connected in series and the third stage is a Schmidt trigger inverter used to eliminate jitter of output frequency as shown in Figure 3. Output inverter stage number 5 is connected to the input inverter stage number one to form a voltage feedback loop as shown in Figure 3, with a buffer stage after the oscillator output inverter stage and the readout oscilloscope equipment.

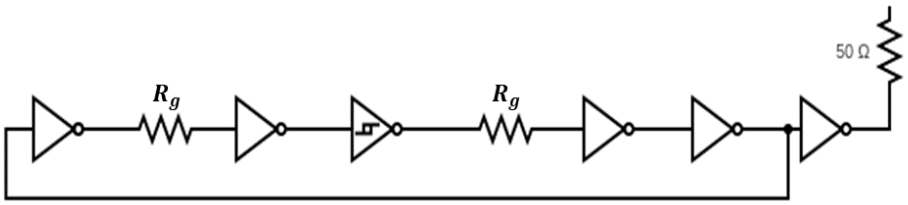

Figure 3: Schematic of the ring oscillator sensing circuit.

Frequency signal of the integrated sensors with the RF ring oscillator circuit can be modelled as follows:

$$Fosc = \frac{1}{2(N * Ron\,(Cd + Cg) + M * Rg * Cg)}, \quad (1)$$

, where N is the number of inverter stages used, M is the number of graphene wafers connected to the ring oscillator circuit, C_g is the gate capacitance, C_d is the drain capacitance, R_g is the initial graphene resistance, and R_{on} is the on-resistance. Generated frequency due to changes in monolayer graphene's resistance can be also modelled as:

$$Fg = \frac{1}{2(N * Ron\,(Cd + Cg) + M * (Rg + \Delta Rg) * Cg)}, \quad (2)$$

and as, $\Delta F = F_{osc} - F_g$:

$$\Delta F = \frac{2 * M * \Delta Rg * Cg}{4(N * Ron(Cd + Cg) + M * Rg * Cg)(N * Ron(Cd + Cg) + M(Rg + \Delta Rg)Cg)}, \quad (3)$$

, so normalized change in frequency ($\frac{\Delta F}{F}$) is modelled as:

$$\frac{\Delta F}{F} = \frac{M\Delta RgCg}{NRon(Cd + Cg) + M(Rg + \Delta Rg)Cg}, \quad (4)$$

, since MOS capacitance is equal to $C_d + C_g$, we can assume that $k = \frac{C_d + C_g}{C_g}$:

$$\frac{\Delta F}{F} = \frac{M\Delta Rg}{KNRon + M(Rg + \Delta Rg)}, \quad (5)$$

,since $\frac{R_g}{R_{on}}$ is way smaller than 1, let's assume $\beta = \frac{KN}{M} + \frac{R_g}{R_{on}}$, which is a complex constant depending on the ratio between gate and drain constants, the ratio between graphene resistance and on resistance and also depending on number of inverter stages and graphene sensors, so after dividing by R_{on} :

$$\frac{\Delta F}{F} = \frac{\frac{\Delta Rg}{Ron}}{\beta + (\frac{\Delta Rg}{Ron})}, \quad (6)$$

, finally as R_{on} is a constant we can consider $\gamma = \beta * R_{on}$:

$$\frac{\Delta F}{F} = \frac{\Delta Rg}{\gamma + \Delta Rg}, \quad (7)$$

, and the γ constant can be represented as:

$$\gamma = \frac{RonKN}{M} + Rg \quad (8)$$

Upon applying physical constant change on the monolayer graphene sensors, the rise and fall times of each inverter in the ring oscillator circuit increases due to the change in the charging and discharging time of the output capacitor at the sensor stage, which leads to the change in the overall ring oscillator frequency. This effect can be easily correlated to resistivity and the applied physical change e.g. gamma irradiation, or bending strains. Transducer design showed perfect results when it comes to selectivity against ambient conditions e.g. light photon, or temperature.

Selectivity of the sensors against light can be modelled by considering light photon effect as an induced error in the frequency reading by using the following equation:

$$\%\ error = \frac{F_{without\ light} - F_{light}}{F_{light}} * 100\ , \quad (9)$$

By calculating the %error due to light photons interacting with monolayer graphene, we can calculate level of uncertainty in ΔR_g at any dose or strain by using the derivative of equation (7) and substitute change in frequency reading when light is applied:

$$\frac{d\Delta R_g}{d\frac{\Delta F}{F}} = \frac{\gamma}{\left(\frac{\Delta F}{F} - 1\right)^2}, \tag{10}$$

Then the uncertainty in can be calculated using the following equation:

$$W_{\Delta Rg} = \left(\left(\frac{d\Delta Rg}{d\frac{\Delta F}{F}}\right)^2 * \left(w_{\frac{\Delta F}{F}}\right)^2\right)^{0.5} \tag{11}$$

Calculating uncertainty in ΔRg were very small, around 0.13% as shown in chapter 3, which is already calculated in correlation with uncertainty in measuring $\frac{\Delta F}{F}$ as shown in equations (9-11), proving that the ring oscillator circuit transducer has a direct impact on selectivity of the sensor platform against incident light photons.

Chapter 3

Monolayer Graphene Radiation Sensor [1]

3.1 Working Principle

As mentioned in the previous chapter, the working principle of most of the solid state or direct radiation sensors mainly depends on capturing signal due to change in Dirac voltage or electric field caused by incident radiation due to Compton scattering. In this work we are proposing a new working principle that depends on induced lattice defects in graphene when subjected to ionizing radiation. These induced defects shift the monolayer graphene from a perfect crystalline material with minimal level of defects density, to a non-crystalline phase with induced defects and interstitials caused by p-doping due to interaction with air molecules while being irradiated with ionizing photonic radiation [89-91]. These changes in monolayer graphene structure causes changes in the electronic property of the graphene, e.g. resistivity.

Our sensor device consists of two monolayer graphene sensors connected to a transduce RF ring oscillator circuit, used in monitoring the change in resistivity and change it into a change in oscillating frequency in response to the incident radiation dose. The framework of the transducer can be described as a reduction in oscillating frequency as a result of resistance increase, and this change in oscillating frequency can be estimated by equation (7):

$$\frac{\Delta F}{F} = \frac{\Delta R_g}{\gamma + \Delta R_g},$$

Where γ is a complex constant that be estimated by equation (8):

$$\gamma = \frac{R_{on} K N}{M} + R_g ,$$

Using equation (8), γ was calculated to be 37.7 kΩ.

[1] This work has been presented in a paper with the title of "Monolayer Graphene Radiation Sensor with Backend RF Ring Oscillator Transducer" [101]

This new concept of radiation detection embraces the fabricated sensing material selection from the constraints of having extremely high Z number or atomic number, and also make use of the induced defects on the microstructure and atomic level as it's the main cause of the electronic change measured by the sensor. Moreover, the sensor itself can be easily tailored as wearable sensor due to its low volume as no large thicknesses are needed in the new approach. As monolayer graphene has extremely high carrier mobility, which allows for high conductivity, sensitivity, and selectivity toward ionizing radiation, it was chosen as a sensing element to the radiation sensor. Backend circuit also played a role in suppressing environmental background effect caused by incident light photons, by integrating two graphene sensors as shown in Figures

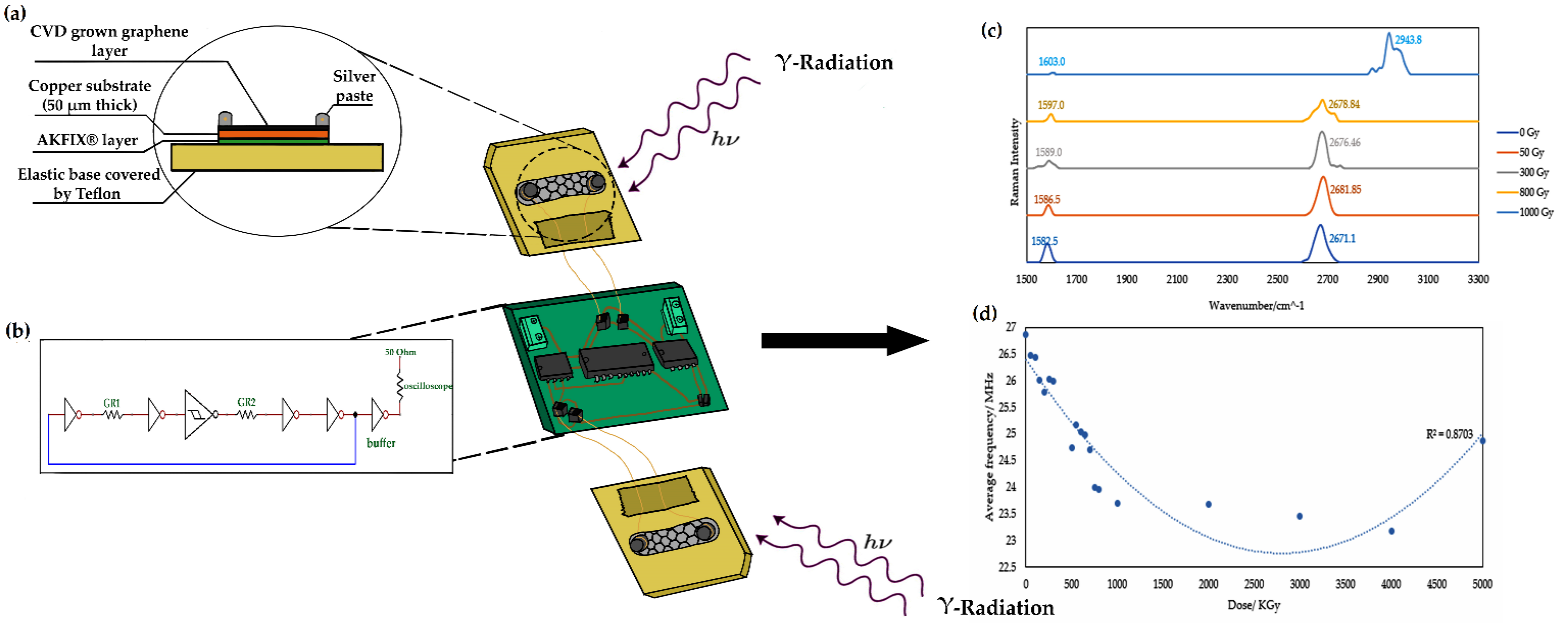

Figure 4: Schematic summarizing the working criteria for the proposed radiation sensor. (a) A cross section through the graphene-based sensing part. (b) RF ring oscillator circuit design. (c) Raman spectra of graphene after irradiation at different doses. (d) Average frequency plot vs. the applied irradiation dose, showing a drop in average frequency after irradiation.

3&4, which amplifies the signal produced by the incident radiation in comparison with the response of the ambient light photons.

3.2 Materials

CVD or chemical vapor deposition grown monolayer Graphene on a 50-micron thick copper foil was used in fabrication of the two sensing elements shown in Figure 4 (a)&(b). The mentioned Graphene was purchased from 2D Semiconductors placed in Scottsdale, AZ, USA. CVD process allows for a chemisorption reaction to occur over the substrate forming stable monolayer graphene without being affected by vacancy point defect concentrations which may furtherly affect the initial readings of the sensor.

Chemical vapor deposition process of growing monolayer graphene starts with temperature elevation to around 1035°C, where hydrogen gas is pumped in a constant flow in parallel with annealing, followed by a process of 3h growth using a mixture of hydrogen and methane at elevated temperatures again. Finally, rapid cooling is done by opening the furnace door. In some cases, graphene is to be transferred to another substrate so van der Waals bonds has to be eliminated, to do so, graphene is subjected to humidity for two days to allow copper oxidation and van der Waals bonds weakening. In our case, van der Waals bonds are needed and transferring graphene isn't favored because the substrate, copper in our case, will be used in stopping the radiation [93].

3.3 Fabrication and Methodology

As shown in Figures 3&4, the two graphene sensors are connected to the RF ring oscillator circuit which is mainly dependent on the number of inverters used. It was found that a series of odd numbered inverters is needed to correlate the change in resistance signal caused by induced defects due to radiation, into a change in oscillating frequency. This change in oscillating frequency is quantified as a signal and compared to the amount of the corresponding irradiation dose.

3.3.1 Sensor Fabrication

Fabrication process starts mainly with mechanical shear cutting of Graphene/Cu sheets into rectangular wafer with area size of 30 mm^2. In parallel to shear cutting procedure a base made of strengthened Kapton tape was fabricated by adding paper to the core of the base covered with Kapton tape from all sides to form an elastic base with a surface area of 25 cm^2. This elastic based was mainly designed and fabricated to allow easy access to the graphene wafer without holding it, but holding the base instead so not to damage the graphene layer. The pre sheared Graphene/Cu wafers are fixed to the elastic based via acrylonitrile AKFIX® binder. This fixation procedure is applied to eliminate any slipping that might occur due to handling loads. AKFIX® binder is widely used in multiple sensors applications such as strain gauges and is used as a reliable binder in sensors research.

0.1 cm^3 drop of the binder was added over the elastic base then the Graphene/Cu wafer is placed carefully over the drop so not to allow the binder to overflow over the Graphene deposited side of the wafer, which might damage the monolayer graphene completely. Electrical connections were mostly based on silver paste connections, which connects Cu wiring to the graphene surface and from graphene surface to the transducer circuit. Conductive Silver paste consists of three main components: conductive silver particles having a weight percent of 60wt%, auxiliary agent, and volatile solvent which evaporates upon curing.

Two 0.15 cm^3 drops of silver paste are added to preplaced copper wires over the graphene wafer surface, drop at each edge as shown in Figure 4(a). Two 0.15 cm^3 pre-cured drops of the silver paste are added over the graphene surface on the far ends of the wafer after being well mixed, then copper wires are fixed in the silver paste so that it's positioned in the middle of the drop upon curing. Silver paste was then left to cure in room temperature for a period of 16 to 20 hours rather than 30 minutes at 120°C to 200°C to avoid any high temperature, so not to destroy monolayer graphene surface [94].

3.3.2 Gamma and Beta Irradiation

Two Graphene wafer sensors are irradiated with the same dose of irradiation to achieve accumulative dose, thus the needed change in crystal structure and change in resistance. This procedure was made separately away from the transducer, and after specific time of irradiation after achieving the needed dose equally to the two sensors, both are assembled to the transducer subsequently for frequency readout signal generation. Gamma irradiation was applied using a Co-60 source between 0 to 1KGy, followed by transducer circuit generation. The same irradiation procedure was repeated but with beta irradiation on two different sensors, with an irradiation dose ranging between 0 to 9 kGy.

3.3.3 Spectroscopy and Characterization

As the working principle of the proposed sensor is mainly dependent on the material interaction, or induced defects in monolayer graphene due to incident radiation, material defects has to be enumerated and characterized. The main primary characterization technique used in our study is Raman spectroscopy which characterizes changes in lattice structure reflecting changes in Dirac point and electron mobility through the graphene sheet by studying vibrational excitations of graphene bonds resulting from inelastic scattering of photons. Billerica, MA USA, a Bruker produced dispersive Raman spectroscopy machine was used. Irradiated graphene samples were characterized using 20 mW, 532 nm laser source with 50 x 1000 µm aperture.

Morphology of graphene sheets were also characterized using scanning electron microscopy (SEM) to study cracks and deformations caused by incident radiation on graphene flakes scale, which is considered as intermediate between micro and macroscale characterization. Field emission scanning electron microscopy (FE-SEM, Zeiss SEM Ultra 60) machine produced by Zeiss. Machine with used with magnitudes ranging between X250 to X1500, working distance of 4.9 mm and high-tension value of 4kV.

3.4 Results and Discussion

3.4.1 Raman Spectroscopy Analysis

As mentioned in the previous subsection, Raman spectroscopy was used to study vibrational excitation of graphene bonds due to inelastic scattering of photons to reflect on the amount of lattice destruction of defects induced by incident ionizing radiation. Three main sharp peaks are analyzed and studied carefully to assess the level of crystallinity and quality of the graphene sheet after every irradiation step: G peak, D peak, and 2D peak [95]. Intrinsic graphene sheets demonstrate sharp peaks as shown in Figure 5, G, D and 2D peaks are located at wavelength of 1582.7 cm^{-1}, 1350 cm^{-1} and 2671.11 cm^{-1} respectively, and with $\frac{I_{2D}}{I_G}$ ratio of 1.99, which indicate a high quality deposited graphene, fabricated under controlled conditions according to literature. $\frac{I_{2D}}{I_G}$ ratio indicates also that the copper substrate of the graphene wafer is of a (111) crystal orientation, according to a study by Frank et al., which mentions the difference between Raman spectra results under different crystal orientations of copper substrates [96].

It was observed that shifting of G and 2D peaks increases at higher doses of ionizing radiation as long as broadness or distortion in the peak itself after irradiation. This effect can be mainly attributed to p-doping, caused by interaction of ionizing radiation with oxygen in air, which breaks bonds and causes stacking of broken graphene layer over each other. Raman analysis was mainly based on the intensity ratio between D-peak and G-peak $\frac{I_D}{I_G}$, and the mentioned shift of peaks. Both the ratio and the shifts, can be used to enumerate and interpret the effect of cumulative irradiation dose on the crustal structure and electronic properties such as bandgap. As shown in table 1, defects density were calculated using $\frac{I_D}{I_G}$ using this Equation:

$$N_D = \left(1.8 \pm 0.5 * \frac{10^{22}}{\lambda_L^4}\right) * \left(\frac{I_D}{I_G}\right) \quad (12)$$

Where, N_D is the defects density caused by irradiation, λ_L is the wavelength of the laser in nm.

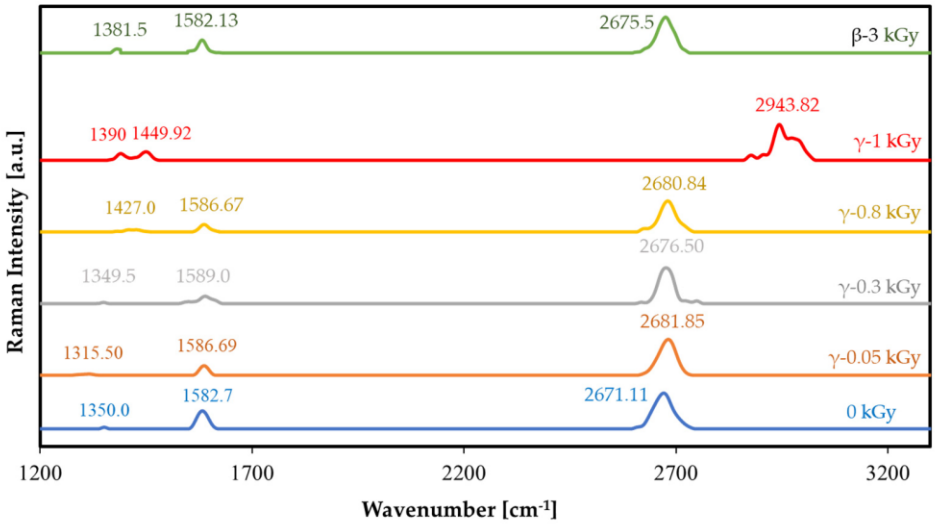

Figure 5: Normalized Raman spectra of CVD-grown graphene on the copper substrate after cumulative gamma irradiation from 0 kGy to 1 kGy.

Values of I_D and I_G were extracted from the Raman spectra shown in Figure 5 for each irradiation dose. It was observed that $\frac{I_D}{I_G}$ ratio increases as gamma irradiation dose increases between 0 to 1 KGy. G and 2D peaks shift was also observed and compared to the intrinsic peak positions of graphene, as shown in Table 1. N_D values or defects density per cm^2 were calculated using Equation (12), showing an increase in the defects density as irradiation dose increases, which is due to the distortion and deformations caused to the hexagonal crystal structure of Graphene in the domains of monolayer deposited Graphene. Those effects cause decrease in electron mobility, and increase in bandgap of graphene, leading to an increase in resistivity which decreases the measured oscillating frequency readout signal generated by the transducer circuit.

Table 1: Raman spectroscopy analysis of CVD-grown graphene layer at the laser wave length of 531 nm for gamma-irradiation doses ranging from 0 to 1 kGy and beta-irradiation doses between 0 and 3 kGy.

Type of irradiation	**Irradiation Dose [kGy]**	$\frac{I_D}{I_G}$	**D-peak shift** $[cm^{-1}]$	**G-peak shift** $[cm^{-1}]$	**2D-peak shift** $[cm^{-1}]$	$N_D\left[\frac{defects}{cm^2}\right]x10^{11}$
Gamma Irradiation	0	0.088	-	-	-	0.198
	0.05	0.118	-34.5	+3.99	+10.74	0.265
	0.3	0.162	-0.5	+6.30	+5.39	0.364
	0.8	0.293	+77	+3.97	+9.73	0.658
	1	0.792	+40	-132.8	+252.71	1.780
Beta Irradiation	3	0.304	+31.5	-0.57	+4.39	0.683

Another observation regarding the Raman spectra outputs is the broadness of the 2D peak increased with increasing cumulative radiation dose, resembling the layering effect caused by cracking and stacking of monolayer graphene into multiple layers [97]. Raman spectroscopy was repeated in the same way for beta irradiation, as shown in Figure 5, where 3 kGy of cumulative beta radiation led to a calculated $\frac{I_D}{I_G}$ of 0.304, which is almost equivalent to $0.683 * 10^{11}$ defects per cm2. This defect density is lower than that caused by 1 kGy of gamma irradiation, proving that the physical lattice changes caused by beta irradiation of the graphene are much lower than the effects induced by gamma irradiation. This can also be attributed to ozone adsorption caused by beta irradiation without a vacuum, causing a p-doping effect that is lower than that caused by gamma irradiation [90].

3.4.2 Morphological Characterization

Figure 6 shows SEM images of the graphene morphology before and after gamma irradiation with different doses ranging between 0.5 and 3 kGy. The SEM images showed that the CVD graphene domains grew in a dendritic pattern. The graphene nuclei are highlighted by green circles in Figure 6(b). Lattice lines are also shown in the zoomed SEM image in Figure 6(b) (highlighted by the red box), with copper substrate surrounding the graphene domains. Figure 6(c-e) show the morphology of 0.5 kGy gamma-irradiated graphene, clearly showing the evolution of the microstructural defects at the domain level and the increase in defect number, size, and distribution. Figure 6(c-e) shows the emergence of wrinkles (highlighted by blue circles in Figure 6(e) caused by gamma irradiation.

Wrinkles could be observed as light-grey lines inside the domain and are outlined by blue circles in the zoomed-in Figure 6(e). Figure 6(f,g) shows that these wrinkles further evolve into cracks after 1 kGy of irradiation, verifying the dramatic increase in defect density after 0.8 kGy that was observed in the Raman analysis. The cracks can be observed as dark lines. Beyond 1 kGy of gamma irradiation, the generated cracks developed into denser and thicker channels, as shown in Figure 6(h) for the 3 kGy irradiated graphene. Figure 6(h) also shows that these channels became more continuous and interconnected compared to the 1 kGy case.

Figure 7 shows an SEM image of the graphene sensor after a beta-irradiation dose of 3.5 kGy, showing the defects induced by beta irradiation. As can be seen in Figure 7, compared with gamma irradiation, beta irradiation affected the graphene less in terms of microstructural defects, manifested by fewer wrinkles and less cracking, as shown in Figure 7(b). The observed defects for 3.5 kGy of beta irradiation were lower than for 1 kGy of gamma irradiation (cf. Figure 6(f,g)), which is in line with the calculated defect densities listed in Table 1.

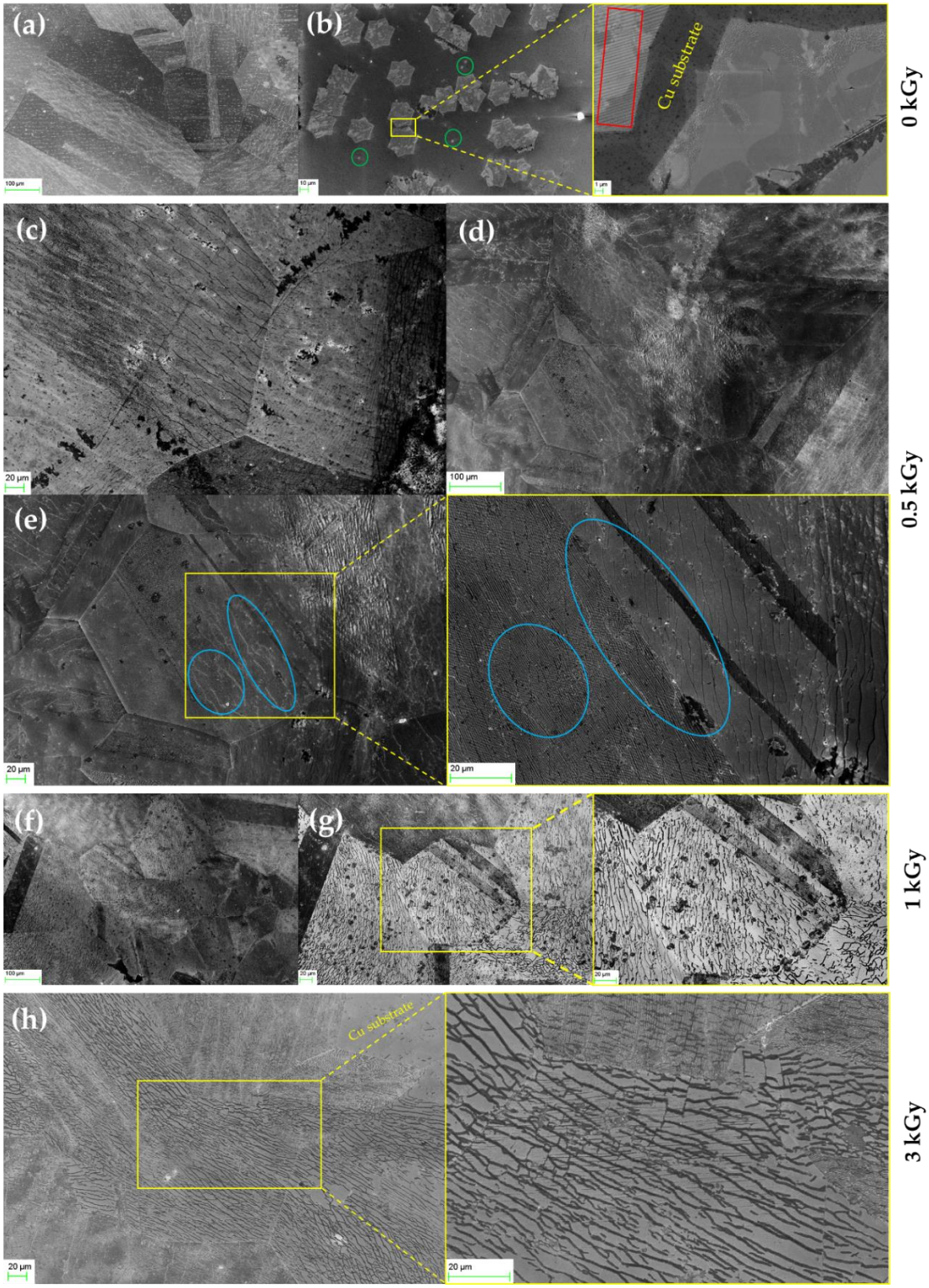

Figure 6: SEM images of CVD-grown graphene. (a,b) before and (c-h) after gamma irradiation. (a,b) Before irradiation (graphene nuclei shown in green circles and lattice lines highlighted in red box). (c-e) After 0.5 kGy irradiation (wrinkles highlighted in blue circles), (f,g) After 1 kGy irradiation, showing thick crack lines evolved. (h) After 3 kGy, showing thicker interconnected crack lines in the graphene domains.

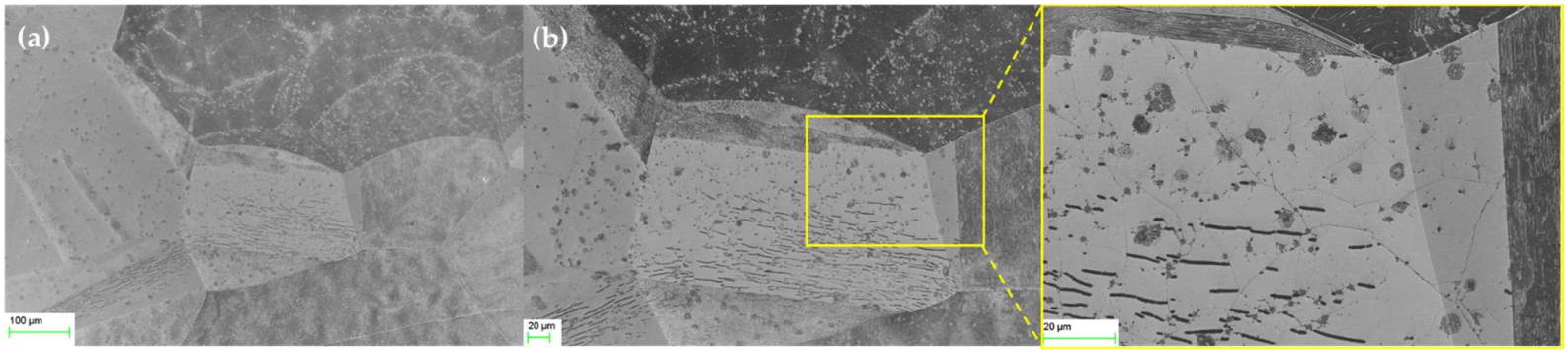

Figure 7: SEM images of (a) graphene after 3.5 kGy beta irradiation. (b) Zoomed-in image showing induced cracks on graphene after beta irradiation

3.4.3 Study of Ambient Light Effect

An experiment was conducted on our sensor assembly in order to determine the impact of light photons on the oscillating output frequency generated by the RF ring oscillator circuit under different light conditions, where cumulative gamma-radiation doses ranging from 0.8 kGy to 1 kGy were applied to the two graphene sensors and oscillating frequency readings were recorded from the oscilloscope under three different environmental conditions: (i) with the two graphene films subjected to light, (ii) with one graphene film subjected to light and the other kept in darkness, and (iii) with both graphene films kept in darkness.

As shown in Figure 8, the % error of each dose was calculated under two different light conditions and plotted in one figure, using equation (9):

$$\%\ error = \frac{F_{without\ light} - F_{light}}{F_{light}} * 100\ ,$$

The results showed an average % error of 0.451% in the case of two graphene sensors in darkness and 0.457% in the case of one graphene sensor in light and the other in darkness, proving the ability of the RF ring oscillator backend circuit used to eliminate the background effects, thus proving it has high selectivity with respect to ambient light photons.

Furthermore, uncertainty calculations regarding the ambient light effect were performed using the % error measurements and the derivative of Equation (7):

$$\frac{d\Delta R_g}{d\frac{\Delta F}{F}} = \frac{\gamma}{\left(\frac{\Delta F}{F} - 1\right)^2},$$

where $\frac{\Delta F}{F}$ was experimentally determined, together with its error due to the background light effect, and $\frac{\Delta F}{F}$ = 0.026899537 ± 0.0032679151 at 0.8 kGy. The light error value in $\frac{\Delta F}{F}$ was subsequently substituted into equation (11) to calculate the uncertainty in the change in graphene resistance due to background light, $W_{\Delta R_g}$:

$$W_{\Delta Rg} = \left(\left(\frac{d\Delta Rg}{d\frac{\Delta F}{F}} \right)^2 * \left(w_{\frac{\Delta F}{F}} \right)^2 \right)^{0.5}$$

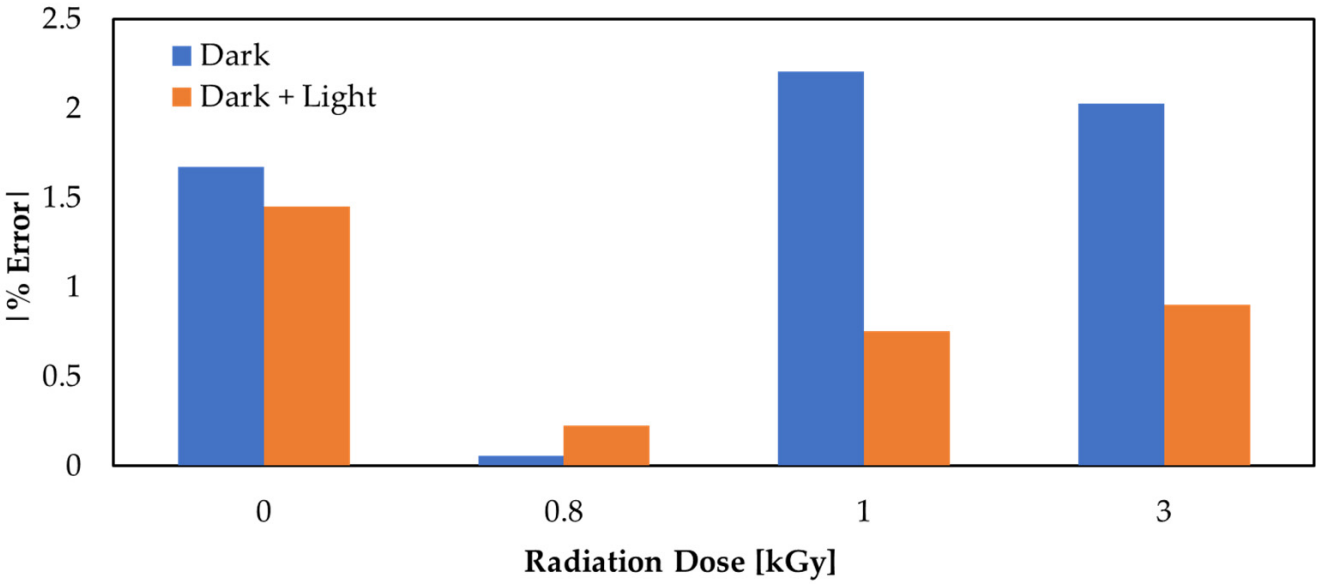

Figure 8: The relationship between %error and dosage in two different light modes.

The uncertainty in ΔR_g was 1.344 Ω, which represents 0.1301058% difference from the calculated ΔR_g at irradiation dose of 0.8 kGy.

3.4.4 Backend RF Ring Oscillator Characterization

After each cumulative dose, the irradiated graphene sensors were subsequently connected to the backend circuit to measure the percentage change in the oscillating frequency. Cumulative gamma irradiation was applied between 0.05 Gy and 1 kGy. As shown in Figure 9, an overall linear trend can be fitted in the range up to 1 kGy, with an average sensitivity that can be determined by taking the slope of the curves. This was found to be a 7.86% change in frequency per kGy, calculated from the curve in Figure 9(a), which corresponds to a change in resistance ΔR_g of 3.82 kΩ/kGy, calculated from the curve in Figure 9(b). It was observed that the standard deviation in the output reading increased rapidly beyond the 1 kGy limit, and the readings

began to deviate from linearity at ~1 kGy. This can be correlated with the SEM images and the calculated defect densities in Table 1 for the 1 kGy and the 3 kGy doses (cf. Figure 6(f-h) and Table 1), which exhibit nonlinear increases in lattice and microstructural defects after 1 kGy. Figure 9(c) shows the effect of the evolution of lattice defects (expressed as lattice defect density) on the graphene's resistivity and the output change in frequency.

Furthermore, the RF ring oscillator circuit was used to characterize the beta-irradiated radiation dose ranging between 0 and 9 kGy) graphene sensors. Figure 10 shows the linear relation between radiation value and % change in frequency, provided the change in frequency results from irradiation in the range between 0 and 9 kGy. The average sensitivity of the sensor to beta irradiation showed a change in Rg per Gy of 0.12 kΩ/kGy and % change in frequency per kGy of 0.29%, showing that the sensor was 27.1 times less sensitive than for gamma radiation. This is suggested to be due to the effect of the beta irradiation taking place in an ambient environment, without applying a vacuum, allowing further adsorption of the ozone which is usually located in the electron beam and hence causing a p-doping effect to occur but with lower density than for gamma irradiation which can also attributed to the lower energy of incident beta irradiation than gamma irradiation, causing a lower change in resistance than for gamma radiation [92].

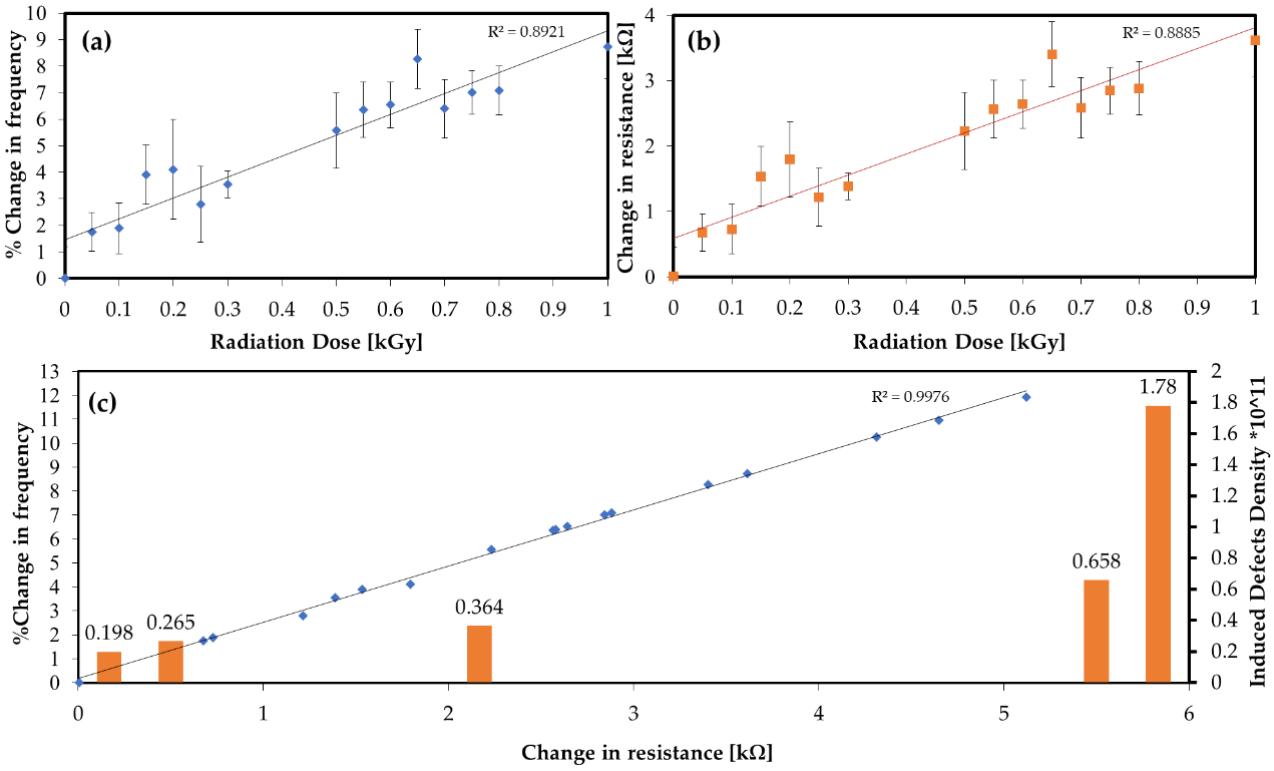

Figure 9: The relation between cumulative gamma-radiation dose with (a) %change in frequency and (b) change in graphene resistance ΔR_g. (c) Relation between change in graphene

resistance and % change in frequency, showing the corresponding induced defect density.

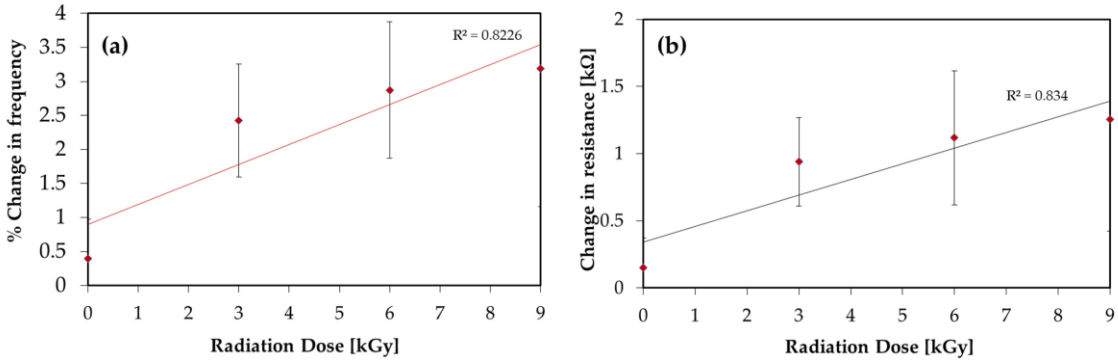

Figure 10: (a) The relationships between cumulative beta-irradiation dose and % change in frequency, and (b) change in resistance, ΔR_g.

3.4.5 Comparison with other Graphene based Sensors

Table 2: Comparison between different graphene based radiation sensors

Author Reference	Backend Platform	Detection Principle	Sensitivity	Disposability	Dose rate	Dose range	Dose Source	Application
Jain et al.	GFET	Dosimeter	1 V/kGy	Disposable	8 kGy/hour	1-20 kGy	Co-60 (Gamma)	Food industry
Feizei et al.	Conductive Cell	Dose Rate Detection	0.0708 min/mGy	Not Disposable	0.00294-0.01182 kGy/hour	50-130 mGy/min	Co-60 (Gamma)	Diagnostic activities
This work (Gamma)	RF Ring Oscillator Circuit	Dosimeter	3.82 kΩ/kGy	Disposable	0.885 KGy/hour	0.05-1 kGy	Co-60 (Gamma)	Food industry and homeland security
This work (Beta)	RF Ring Oscillator Circuit	Dosimeter	0.12 kΩ/kGy	Disposable	90 J/s	0 to 9 kGy	Particle Accelerator	Food industry and homeland security

In comparison with graphene based radiation sensors in literature, it was observed that our work used moderate dose rates and dose range, which is sufficient in multiple applications such food industry, and homeland security. Moreover, our sensor achieved the highest sensitivity in gamma and beta detection with the linearity needed for sensor reliability. Selectivity against environmental effects, e.g. light and temperature, was achieved by the connected backend circuit used which is RF ring oscillator circuit. This platform design achieved scalability when it comes to the used of graphene, independent of any defects density induced originally in graphene's structure.

Chapter 4

Monolayer Graphene Strain Sensor [2]

4.1 Working Principle and Fabrication

The proposed sensing approach is summarized in Figure 11, The strain was applied to the graphene on-Cu samples by the method of standard bending jigs, and the change in graphene resistivity. Change in monolayer graphene resistivity due to strain can be directly attributed to structure deformation caused by elongation of graphene's bonds due to applied bending forces, which in return causes changes in electrical properties and band structure in an electromechanical response. As a result, the rise and fall times of each inverter in the ring oscillator circuit increases due to the change in the charging and discharging time of the output capacitor at the sensor stage, which leads to the change in the overall ring oscillator frequency. Finally, the percentage change in frequency could be correlated to the resistivity and strain of the sensing element. All of the applied strains are in the elastic region of the graphene sheets, which reflects on the sensitivity of graphene to low level of strains.

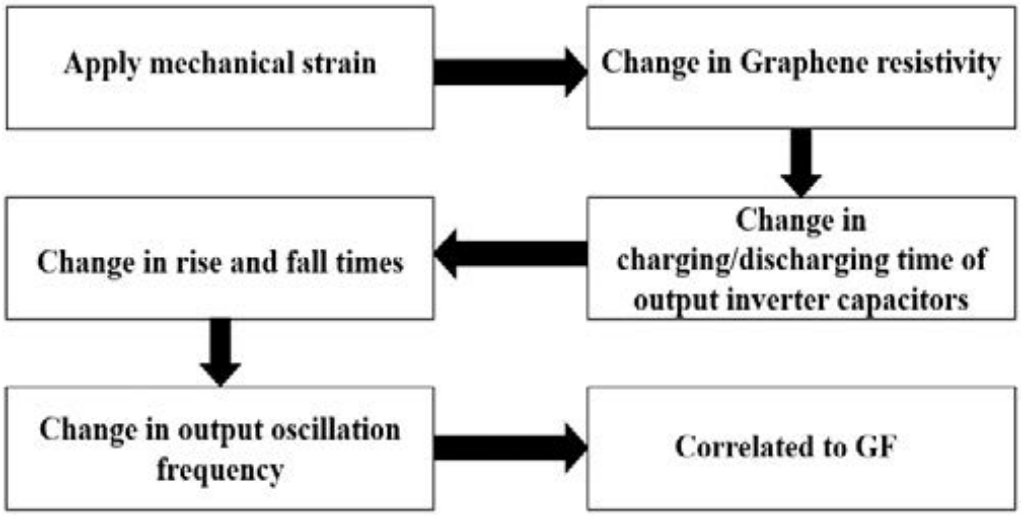

Figure 11: Summary of the working principle of the strain sensor.

Fabrication process was the same as mentioned in chapter 3 with the same materials and design. The paper/Teflon elastic base which is assembled using acrylonitrile binder to the Graphene/Cu wafer is mainly used in here to overcome any slippage between the wafer and

[2] This work has been presented in a paper with the title of "RF Ring Oscillator Graphene-based Strain Sensor" [102]

the base, and to ensure that the base is returning to its original shape after releasing stresses. Similar copper wiring connections were added to the surface of the graphene wafers from both edges using silver pastes connections, cured under ambient conditions. Both wirings are connected to the RF ring oscillator circuit described in chapter 2, and two of the graphene sensors sheets are connected to the circuit to induce the needed frequency signal in correlation with the applied strain.

4.2 Results and Discussion

Pure bending jigs are designed and manufactured using precise EDM cutting with different curvatures. Each curvature corresponds to a specific strain calculated using the curvature and the thickness of the whole sensor. Generated strains by the bending jigs are ranging between $8.32 * 10^{-4}$ to $16.61 * 10^{-4}$. Those strain levels are considered to be in the elastic level of graphene and are highly needed in robotic application and other multiple fields. Resistance increase in the range of 0.24 Ω to 0.28 Ω was observed over a range of applied strains from 0.083% to 0.248%, which reflects the impact of mechanical stress on the graphene's bandgap as reported in previous works [98], showing that as strain increases, the lattice structure of graphene is stretched. Internal covalent bond lengths increase, causing the bandgap to widen, increasing the needed energy for electrons to jump from valence band to conduction band [98-100]. This was further confirmed by the change in resistivity, which was in the order of 1.6 Ω/□, to 1.87 Ω/□, as shown in Figure 12.

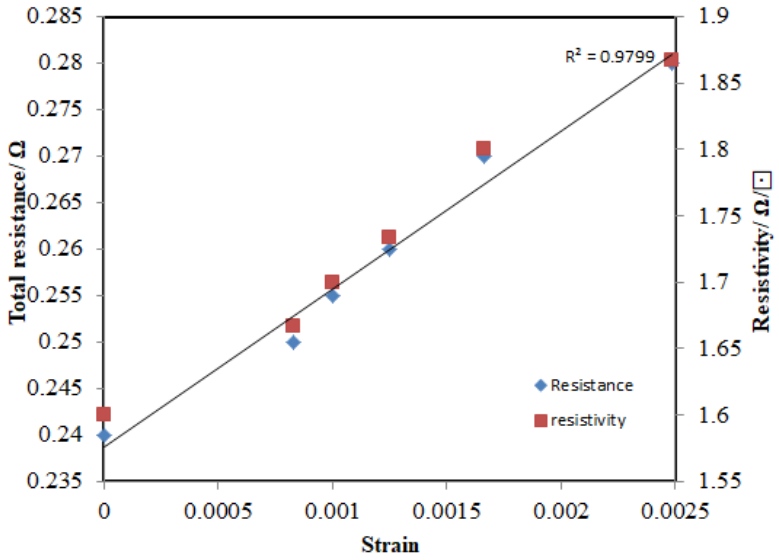

Figure 12: Relation between Applied strain and CVD-grown graphene resistance, and resistivity.

The sensitivity of the RF ring oscillator technology can be represented by demonstrating the effect of changing graphene resistance on the output % change in frequency which shows that

change in resistance from +0.01 Ω to +0.04 Ω has caused a change in the output frequency in the order of 5.56% to 7.69%, at an overall circuit sensitivity of 0.71% change in frequency per 0.01 Ω as shown in Figure 13.

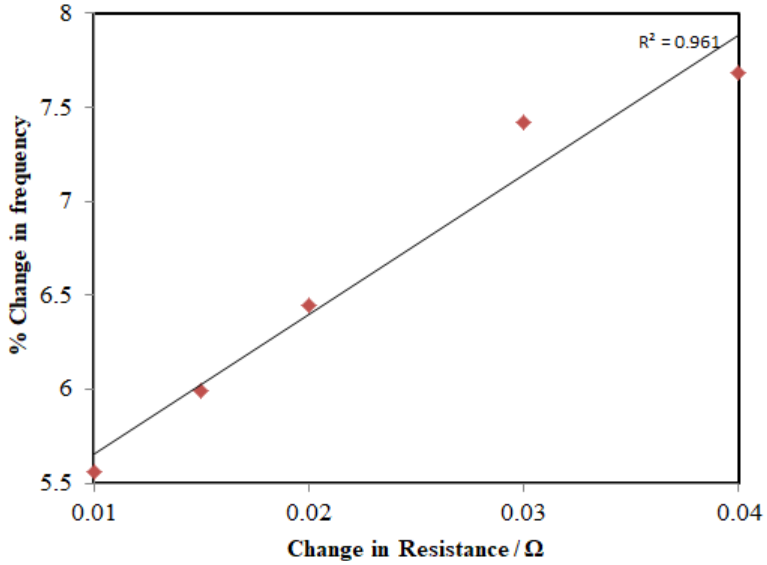

Figure 13: Relation between CVD-grown graphene's resistance and % change in output frequency.

Change in strain from 0.083% to 0.248% caused a change in monolayer graphene resistance ($\frac{\Delta R}{R}$) in the order of 4.2 to 17%, as shown in Figure 14. Hence, the average gauge factor can be extracted from the figure by calculating the average slop of the fitted line to be GF ≈ 64.36.

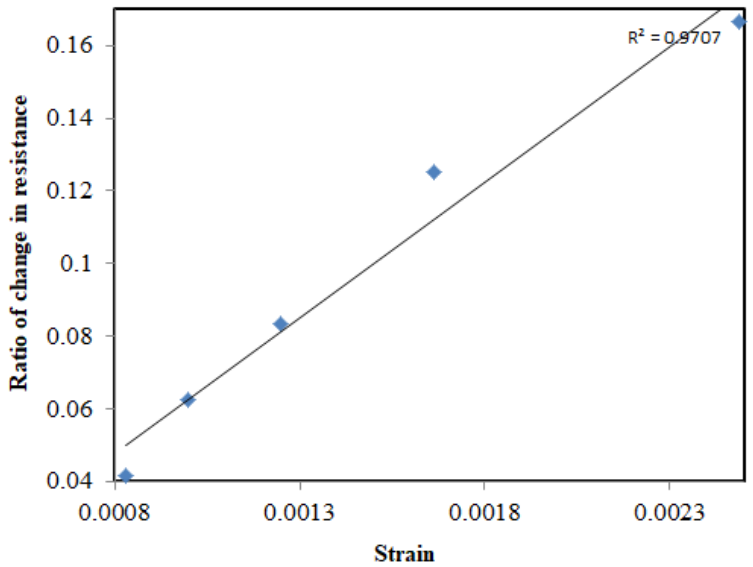

Figure 14: Relation between CVD-grown graphene's resistance and % change in output frequency.

Table 3 summarizes the effects of the applied strain on the GF and normalized frequency change. It is clear that GF ranging from ~ 50 to 75 after 3 experimentation cycles ensuring similar performance after each test. GF seems to be at it highest levels in the range of $12.47 * 10^{-4} to\ 16.61 * 10^{-4}$ strain range. GF was calculated from a derived equation using Equation 7 as follow:

$$GF = \frac{\frac{\Delta R_g}{R_g}}{\varepsilon} = \frac{\gamma * \frac{\Delta F}{F}}{\varepsilon * R_g * (1 - \frac{\Delta F}{F})} \tag{13}$$

,where ε is the applied flexural strain.

Table 3: Gauge factor vs. strain and normalized frequency change.

Strain ($\boldsymbol{x10^{-4}}$)	**Effects on GF and Normalized Frequency**	
	GF	$\boldsymbol{\frac{\Delta F}{F}}$
8.32	50.08	0.0556
9.98	62.62	0.0599
12.47	66.83	0.0644
16.61	72.25	0.0742

Chapter 5

Conclusion

We introduced sensing platform consists of 2 CVD-grown monolayer graphene sensors integrated with RF ring oscillator circuit as a transducer circuit. This transducer circuit generates a readout frequency signal as response to a physical change applied to the two sensors, e.g. ionizing radiation, and flexural strain. The mentioned design allows the fabricated sensors to be scalable, and highly selective against environmental effects such as: light photons and temperature. These novelties make the proposed platform overcome problems reported in literature for solid state radiation detectors such as:

- Dependency of thickness or volume on atomic number of used elements.
- Fading signal problems.
- Mild cooling is needed while using some materials e.g. Germanium and while using specific nodes or connections such as Schottky nodes.
- Difficulties in growing single crystals, which is needed for higher electrons mobility.
- Ion migration and phase transformation due to structural instability.
- Toxicity of some of the used elements.

Using of CVD-grown monolayer graphene in flexural strain sensing is considered a new approach of using structural deformations in graphene as the main source of change to be transformed into a signal, rather than the most commonly used tunneling effect of electrons through dispersed graphene domains. Similarly, this approach was able to fill the gap and surpass the reported problems of using tunneling effect among neighboring sheets method such as:

- Dependency on graphene domains dispersion, which affects the quality of graphene and cause induced defects.
- Lower gauge factors at lower strain ranges, due to the small changes in distances between graphene domains.
- Lower gauge factors in flexural strain sensing, as a result of created conductivity channels.

Change in resistivity of graphene due to the applied Physical changes applied on the graphene's surface are mainly coupled with change in frequency signals as mentioned in chapters 3 & 4, and the key findings are:

- The average sensitivity to gamma radiation detection is 3.82 kΩ/kGy, which corresponds to change in frequency of 7.86 $\%kGy^{-1}$ in response to cumulative gamma

radiation dose ranging from 0 to 1 kGy

- Insignificant error in frequency measurement due to light is of the order of 0.46%, leading to uncertainty.
- The uncertainty in readings due to background light was analyzed, and the error in the resistance was found to be in the order of 1.34 Ω.
- The average gauge factor in response to flexural strains ranging between $8.32 * 10^{-4}$ to $16.61 * 10^{-4}$ is in the order of 64.36, which corresponds to a change in frequency of 7.42%, achieving a sensitivity of around 3 times higher than the mentioned flexural strain sensitivities in the same strain range.

Through these lines, we are proposing some future enhancements and proposed ideas to enhance the introduced sensor platform such as replacement of flexible Teflon base with PDMS base to better implement the sensor platform as a wearable one. Adding PDMS base will also allow for monolayer graphene transfer over its surface easily using PMMA transfer method. Monolayer graphene can be patterned on the substrate to allow for complex strain sensitivity.

References

[1] R. Bogue, "Graphene sensors: A review of recent developments," *Sens. Rev.*, vol. 34, no. 3, pp. 233–238, 2014.

[2] E. W. Hill, A. Vijayaragahvan, and K. Novoselov, "Graphene sensors," *IEEE Sens. J.*, vol. 11, no. 12, pp. 3161–3170, 2011.

[3] S. Dhanekar and K. Rangra, "Wearable Dosimeters for Medical and Defence Applications: A State of the Art Review," *Adv. Mater. Technol.*, vol. 6, no. 5, pp. 1–15, 2021.

[4] S. Grdanovska, R. Briber, and T. Koeth, "CHARACTERIZATION OF RADIATION DAMAGE TO A NOVEL PHOTONIC CRYSTAL SENSOR," University of Maryland, College Park, 2015.

[5] F. Liu *et al.*, "Recent Progress in Halide Perovskite Radiation Detectors for Gamma-Ray Spectroscopy," *ACS Energy Lett.*, vol. 7, no. 3, pp. 1066–1085, 2022.

[6] F. Sizov, "THz radiation sensors," *Opto-Electronics Rev.*, vol. 18, no. 1, pp. 10–36, 2010.

[7] R. Speller, A. Olivo, S. Pani, and G. Royle, "Biomedical Sensors of Ionizing Radiation," *Biomed. Sensors*, no. 1994, pp. 129–238, 2009.

[8] C. Leroy, "Review of radiation detectors," *AIP Conf. Proc.*, vol. 958, no. November 2007, pp. 92–100, 2007.

[9] N. Security and S. Series, *New Techniques for the Detection of Nuclear and Radioactive Agents NATO Science for Peace and Security Series*, no. May. 2015.

[10] C. J. Nielsen, "Radiation safety certification: A review," *J. Nucl. Med. Technol.*, vol. 46, no. 4, pp. 321–325, 2018.

[11] A. Tarancón, H. Bagán, and J. F. García, "Plastic scintillators and related analytical procedures for radionuclide analysis," *J. Radioanal. Nucl. Chem.*, vol. 314, no. 2, pp. 555–572, 2017.

[12] A. Karmakar, J. Wang, J. Prinzie, V. De Smedt, and P. Leroux, "A Review of Semiconductor Based Ionising Radiation Sensors Used in Harsh Radiation Environments and Their Applications," *Radiation*, vol. 1, no. 3, pp. 194–217, 2021.

[13] G. R. Gilmore, "Practical Gamma-ray Spectrometry."

[14] M. K. Hossain *et al.*, "Current Applications and Future Potential of Rare Earth Oxides in Sustainable Nuclear, Radiation, and Energy Devices: A Review," *ACS Appl. Electron. Mater.*, vol. 4, no. 7, pp. 3327–3353, 2022.

[15] S. Kaya, E. Yilmaz, A. Kahraman, and H. Karacali, "Frequency dependent gamma-ray irradiation response of Sm2O3 MOS capacitors," *Nucl. Instruments Methods Phys. Res. Sect. B Beam Interact. with Mater. Atoms*, vol. 358, pp. 188–193, 2015.

[16] A. Kahraman, E. Yilmaz, A. Aktag, and S. Kaya, "Evaluation of Radiation Sensor Aspects of Er2O3 MOS Capacitors under Zero Gate Bias," *IEEE Trans. Nucl. Sci.*, vol. 63, no. 2, pp. 1284–1293, 2016.

[17] A. Kahraman and E. Yilmaz, "Irradiation response of radio-frequency sputtered Al/Gd2O3/p-Si MOS capacitors," *Radiat. Phys. Chem.*, vol. 139, no. February, pp. 114–119, 2017.

[18] A. Kahraman and E. Yilmaz, " Proposal of alternative sensitive region for MOS based radiation sensors: Yb 2 O 3 ," *J. Vac. Sci. Technol. A Vacuum, Surfaces, Film.*, vol. 35, no. 6, p. 061511, 2017.

[19] P. Sangsingkeow, K. D. Berry, E. J. Dumas, T. W. Raudorf, and T. A. Underwood, "Advances in germanium detector technology," *Nucl. Instruments Methods Phys. Res. Sect.*

A Accel. Spectrometers, Detect. Assoc. Equip., vol. 505, no. 1–2, pp. 183–186, 2003.
[20] S. Shrestha *et al.*, "High-performance direct conversion X-ray detectors based on sintered hybrid lead triiodide perovskite wafers," *Nat. Photonics*, vol. 11, no. 7, pp. 436–440, 2017.
[21] Y. C. Kim *et al.*, "Printable organometallic perovskite enables large-area, low-dose X-ray imaging," *Nature*, vol. 550, no. 7674, pp. 87–91, 2017.
[22] W. Wei *et al.*, "Monolithic integration of hybrid perovskite single crystals with heterogenous substrate for highly sensitive X-ray imaging," *Nat. Photonics*, vol. 11, no. 5, pp. 315–321, 2017.
[23] K. Sakhatskyi *et al.*, "Assessing the Drawbacks and Benefits of Ion Migration in Lead Halide Perovskites," *ACS Energy Lett.*, vol. 7, no. 10, pp. 3401–3414, 2022.
[24] H. Tsai *et al.*, "A sensitive and robust thin-film x-ray detector using 2D layered perovskite diodes," *Sci. Adv.*, vol. 6, no. 15, pp. 1–8, 2020.
[25] L. Li *et al.*, "Enhanced X-ray Sensitivity of MAPbBr 3 Detector by Tailoring the Interface-States Density," *ACS Appl. Mater. Interfaces*, vol. 11, no. 7, pp. 7522–7528, 2019.
[26] H. Wei *et al.*, "Dopant compensation in alloyed CH3NH3PbBr3-x Clx perovskite single crystals for gamma-ray spectroscopy," *Nat. Mater.*, vol. 16, no. 8, pp. 826–833, 2017.
[27] Y. He *et al.*, "Resolving the Energy of γ-Ray Photons with MAPbI3 Single Crystals," *ACS Photonics*, vol. 5, no. 10, pp. 4132–4138, 2018.
[28] Y. He *et al.*, "High spectral resolution of gamma-rays at room temperature by perovskite CsPbBr3 single crystals," *Nat. Commun.*, vol. 9, no. 1, pp. 1–8, 2018.
[29] S. Yakunin *et al.*, "Detection of gamma photons using solution-grown single crystals of hybrid lead halide perovskites," *Nat. Photonics*, vol. 10, no. 9, pp. 585–589, 2016.
[30] Y. He *et al.*, "CsPbBr3 perovskite detectors with 1.4% energy resolution for high-energy γ-rays," *Nat. Photonics*, vol. 15, no. 1, pp. 36–42, 2021.
[31] Y. He *et al.*, "Demonstration of energy-resolved γ-ray detection at room temperature by the CsPBCl3 perovskite semiconductor," *J. Am. Chem. Soc.*, vol. 143, no. 4, pp. 2068–2077, 2021.
[32] A. Maity, C. Das, A. K. Raychaudhuri, A. Saha, and B. Ghosh, "Highly radiation resistant room temperature organic perovskite halide (FAPbI3) crystal for direct detection of gamma-ray photons down to nano curie activity," *J. Phys. D. Appl. Phys.*, vol. 54, no. 45, 2021.
[33] Q. Xu *et al.*, "Detection of charged particles with a methylammonium lead tribromide perovskite single crystal," *Nucl. Instruments Methods Phys. Res. Sect. A Accel. Spectrometers, Detect. Assoc. Equip.*, vol. 848, no. December 2016, pp. 106–108, 2017.
[34] Y. He *et al.*, "Perovskite CsPbBr 3 single crystal detector for alpha-particle spectroscopy," *Nucl. Instruments Methods Phys. Res. Sect. A Accel. Spectrometers, Detect. Assoc. Equip.*, vol. 922, no. January, pp. 217–221, 2019.
[35] K. M. McCall *et al.*, "α-Particle Detection and Charge Transport Characteristics in the A3M2I9 Defect Perovskites (A = Cs, Rb; M = Bi, Sb)," *ACS Photonics*, vol. 5, no. 9, pp. 3748–3762, 2018.
[36] D. Yu *et al.*, "Two-dimensional halide perovskite as β-ray scintillator for nuclear radiation monitoring," *Nat. Commun.*, vol. 11, no. 1, pp. 1–10, 2020.
[37] L. El Bouanani *et al.*, "Solid-State Neutron Detection Based on Methylammonium Lead Bromide Perovskite Single Crystals," *ACS Appl. Mater. Interfaces*, vol. 13, no. 24, pp. 28049–28056, 2021.
[38] F. Montanarella *et al.*, "Highly Concentrated, Zwitterionic Ligand-Capped Mn2+:CsPb(BrxCl1- x)3Nanocrystals as Bright Scintillators for Fast Neutron Imaging,"

ACS Energy Lett., vol. 6, no. 12, pp. 4365–4373, 2021.
[39] P. K. Nayak *et al.*, "Mechanism for rapid growth of organic-inorganic halide perovskite crystals," *Nat. Commun.*, vol. 7, pp. 1–8, 2016.
[40] Y. Fang, Q. Dong, Y. Shao, Y. Yuan, and J. Huang, "Highly narrowband perovskite single-crystal photodetectors enabled by surface-charge recombination," *Nat. Photonics*, vol. 9, no. 10, pp. 679–686, 2015.
[41] M. I. Saidaminov *et al.*, "High-quality bulk hybrid perovskite single crystals within minutes by inverse temperature crystallization," *Nat. Commun.*, vol. 6, no. May, pp. 1–6, 2015.
[42] C. C. Stoumpos *et al.*, "Ruddlesden-Popper Hybrid Lead Iodide Perovskite 2D Homologous Semiconductors," *Chem. Mater.*, vol. 28, no. 8, pp. 2852–2867, 2016.
[43] H. Tsai *et al.*, "High-efficiency two-dimensional ruddlesden-popper perovskite solar cells," *Nature*, vol. 536, no. 7616, pp. 312–317, 2016.
[44] C. C. Stoumpos *et al.*, "High Members of the 2D Ruddlesden-Popper Halide Perovskites: Synthesis, Optical Properties, and Solar Cells of (CH3(CH2)3NH3)2(CH3NH3)4Pb5I16," *Chem*, vol. 2, no. 3, pp. 427–440, 2017.
[45] L. Pedesseau *et al.*, "Advances and Promises of Layered Halide Hybrid Perovskite Semiconductors," *ACS Nano*, vol. 10, no. 11, pp. 9776–9786, 2016.
[46] Y. Yuan and J. Huang, "Ion Migration in Organometal Trihalide Perovskite and Its Impact on Photovoltaic Efficiency and Stability," *Acc. Chem. Res.*, vol. 49, no. 2, pp. 286–293, 2016.
[47] C. C. Stoumpos *et al.*, "Crystal growth of the perovskite semiconductor CsPbBr3: A new material for high-energy radiation detection," *Cryst. Growth Des.*, vol. 13, no. 7, pp. 2722–2727, 2013.
[48] J. Li *et al.*, "Biological impact of lead from halide perovskites reveals the risk of introducing a safe threshold," *Nat. Commun.*, vol. 11, no. 1, pp. 1–5, 2020.
[49] M. Lyu, J. H. Yun, P. Chen, M. Hao, and L. Wang, "Addressing Toxicity of Lead: Progress and Applications of Low-Toxic Metal Halide Perovskites and Their Derivatives," *Adv. Energy Mater.*, vol. 7, no. 15, 2017.
[50] Y. Yan, T. Pullerits, K. Zheng, K. Zheng, and Z. Liang, "Advancing Tin Halide Perovskites: Strategies toward the ASnX3Paradigm for Efficient and Durable Optoelectronics," *ACS Energy Lett.*, vol. 5, no. 6, pp. 2052–2086, 2020.
[51] R. C. Walker, T. Shi, E. C. Silva, I. Jovanovic, and J. A. Robinson, "Radiation effects on two-dimensional materials," *Phys. Status Solidi Appl. Mater. Sci.*, vol. 213, no. 12, pp. 3065–3077, 2016.
[52] S. Jain, A. S. Gajarushi, A. Gupta, and V. R. Rao, "A Passive Gamma Radiation Dosimeter Using Graphene Field Effect Transistor," *IEEE Sens. J.*, vol. 20, no. 6, pp. 2938–2944, 2020.
[53] Patil, A., Koybasi, O., Lopez, G., Foxe, M., Childres, I., Roecker, C., ... & Chen, Y. P. (2011, October). Graphene field effect transistor as radiation sensor. In *2011 IEEE Nuclear Science Symposium Conference Record* (pp. 455-459). IEEE.
[54] S. Feizi, A. Mehdizadeh, M. A. Hosseini, S. A. Jafari, and P. Ashtari, "Reduced graphene oxide/polymethyl methacrylate (rGO/PMMA) nanocomposite for real time gamma radiation detection," *Nucl. Instruments Methods Phys. Res. Sect. A Accel. Spectrometers, Detect. Assoc. Equip.*, vol. 940, no. May, pp. 72–77, 2019.
[55] J. C. F. Millett, N. K. Bourne, and Z. Rosenberg, "On the analysis of transverse stress gauge data from shock loading experiments," *J. Phys. D. Appl. Phys.*, vol. 29, no. 9, pp. 2466–2472, 1996.

[56] J. Zhao, G. Y. Zhang, and D. X. Shi, "Review of graphene-based strain sensors," *Chinese Phys. B*, vol. 22, no. 5, 2013.
[57] L. Wang, K. J. Loh, W. H. Chiang, and K. Manna, "Micro-patterned graphene-based sensing skins for human physiological monitoring," *Nanotechnology*, vol. 29, no. 10, 2018.
[58] Z. Zeng *et al.*, "A coatable, light-weight, fast-response nanocomposite sensor for the in situ acquisition of dynamic elastic disturbance: From structural vibration to ultrasonic waves," *Smart Mater. Struct.*, vol. 25, no. 6, 2016.
[59] Y. Cai *et al.*, "Stretchable Ti3C2Tx MXene/Carbon Nanotube Composite Based Strain Sensor with Ultrahigh Sensitivity and Tunable Sensing Range," *ACS Nano*, vol. 12, no. 1, pp. 56–62, 2018.
[60] A. D. Smith *et al.*, "Electromechanical piezoresistive sensing in suspended graphene membranes," *Nano Lett.*, vol. 13, no. 7, pp. 3237–3242, 2013.
[61] Y. J. Kim, J. Y. Cha, H. Ham, H. Huh, D. S. So, and I. Kang, "Preparation of piezoresistive nano smart hybrid material based on graphene," *Curr. Appl. Phys.*, vol. 11, no. 1 SUPPL., pp. S350–S352, 2011.
[62] X. Zhang, Y. I. Pan, Q. Zheng, and X. Yi, "Time Dependence of Piezoresistance for the Conductor-," *J. Appl. Polym. Sci.*, vol. 38, pp. 2739–2749, 2000.
[63] F. S. Irani *et al.*, "Graphene as a Piezoresistive Material in Strain Sensing Applications," *Micromachines*, vol. 13, no. 1, 2022.
[64] S. M. Choi, S. H. Jhi, and Y. W. Son, "Controlling energy gap of bilayer graphene by strain," *Nano Lett.*, vol. 10, no. 9, pp. 3486–3489, 2010.
[65] G. Cocco, E. Cadelano, and L. Colombo, "Gap opening in graphene by shear strain," *Phys. Rev. B - Condens. Matter Mater. Phys.*, vol. 81, no. 24, pp. 1–4, 2010.
[66] G. Gui, J. Li, and J. Zhong, "Band structure engineering of graphene by strain: First-principles calculations," *Phys. Rev. B - Condens. Matter Mater. Phys.*, vol. 78, no. 7, pp. 1–6, 2008.
[67] J. W. Jiang and J. S. Wang, "Bright and dark modes induced by graphene bubbles," *Epl*, vol. 97, no. 3, 2012.
[68] Y. Lu and J. Guo, "Band gap of strained graphene nanoribbons," *Nano Res.*, vol. 3, no. 3, pp. 189–199, 2010.
[69] P. Taylor, "High Pressure Research : An Ballistic transport properties across nonuniform strain barriers in graphene," no. May 2012, pp. 37–41, 2011.
[70] M. Anas, M. A. Nasir, Z. Asfar, S. Nauman, M. Akalin, and F. Ahmad, "Structural health monitoring of GFRP laminates using graphene-based smart strain gauges," *J. Brazilian Soc. Mech. Sci. Eng.*, vol. 40, no. 8, pp. 1–10, 2018.
[71] S. Lu *et al.*, "Strain sensing behaviors of GnPs/epoxy sensor and health monitoring for composite materials under monotonic tensile and cyclic deformation," *Compos. Sci. Technol.*, vol. 158, pp. 94–100, 2018.
[72] S. Lu *et al.*, "Health monitoring for composite materials with high linear and sensitivity GnPs/epoxy flexible strain sensors," *Sensors Actuators, A Phys.*, vol. 267, pp. 409–416, 2017.
[73] H. Montazerian, A. Rashidi, A. Dalili, H. Najjaran, A. S. Milani, and M. Hoorfar, "Graphene-Coated Spandex Sensors Embedded into Silicone Sheath for Composites Health Monitoring and Wearable Applications," *Small*, vol. 15, no. 17, 2019.
[74] R. Moriche, M. Sánchez, A. Jiménez-Suárez, S. G. Prolongo, and A. Ureña, "Strain monitoring mechanisms of sensors based on the addition of graphene nanoplatelets into an epoxy matrix," *Compos. Sci. Technol.*, vol. 123, pp. 65–70, 2016.

[75] X. Liu *et al.*, "A highly sensitive graphene woven fabric strain sensor for wearable wireless musical instruments," *Mater. Horizons*, vol. 4, no. 3, pp. 477–486, 2017.
[76] W. E. Mahmoud and S. A. Al-Bluwi, "Development of ultrasensitive mechanical strain sensor made of 2D-assembled graphene monolayers aligned parallel into polysilicon nanocomposites," *Sensors Actuators, A Phys.*, vol. 313, p. 112166, 2020.
[77] J. Everard, *Fundamentals of RF Circuit Design*, vol. 2. 2001.
[78] Y. Chiu, H. C. Hong, and P. C. Wu, "Development and characterization of a CMOS-MEMS accelerometer with differential lc-tank oscillators," *J. Microelectromechanical Syst.*, vol. 22, no. 6, pp. 1285–1295, 2013.
[79] C. H. Weng, G. Pillai, and S. S. Li, "A Thin-Film Piezoelectric-on-Silicon MEMS Oscillator for Mass Sensing Applications," *IEEE Sens. J.*, vol. 20, no. 13, pp. 7001–7009, 2020.
[80] S. M. Mortazavi Zanjani, M. Holt, M. M. Sadeghi, S. Rahimi, and D. Akinwande, "3D integrated monolayer graphene–Si CMOS RF gas sensor platform," *npj 2D Mater. Appl.*, vol. 1, no. 1, pp. 1–8, 2017.
[81] P. Petrashin, W. Lancioni, A. Laprovitta, and J. Castagnola, "Embedded Radiation sensor with OBIST structure for applications in mixed signal systems," *JAREE (Journal Adv. Res. Electr. Eng.*, vol. 5, no. 2, pp. 114–119, 2021.
[82] P. Yang, T. Xia, H. Li, and X. Wang, "A temperature insensitive ring oscillator for low power RF communications," *Proc. - 2013 IEEE Int. Conf. Green Comput. Commun. IEEE Internet Things IEEE Cyber, Phys. Soc. Comput. GreenCom-iThings-CPSCom 2013*, pp. 1804–1809, 2013.
[83] S. Soleymani Kebria and H. Ghonoodi, "Increasing power efficiency in the design of a low power and low phase noise CMOS LC oscillator," *Int. J. Circuit Theory Appl.*, vol. 49, no. 1, pp. 18–30, 2021.
[84] C. S. Lam, "A review of the recent development of mems and crystal oscillators and their impacts on the frequency control products industry," *Proc. - IEEE Ultrason. Symp.*, pp. 694–704, 2008.
[85] W. Thommen, "An improved low power crystal oscillator," *Eur. Solid-State Circuits Conf.*, pp. 146–149, 1999.
[86] M. Brownlee, P. K. Hanumolu, U. K. Moon, and K. Mayaram, "The effect of power supply noise on ring oscillator phase noise," *Conf. Proc. - 2nd Annu. IEEE Northeast Work. Circuits Syst. NEWCAS 2004*, pp. 225–228, 2004.
[87] C. L. Dai, "A capacitive humidity sensor integrated with micro heater and ring oscillator circuit fabricated by CMOS-MEMS technique," *Sensors Actuators, B Chem.*, vol. 122, no. 2, pp. 375–380, 2007.
[88] C. L. Dai, P. W. Lu, C. Chang, and C. Y. Liu, "Capacitive micro pressure sensor integrated with a ring oscillator circuit on chip," *Sensors*, vol. 9, no. 12, pp. 10158–10170, 2009.
[89] A. Ansón-Casaos *et al.*, "The effect of gamma-irradiation on few-layered graphene materials," *Appl. Surf. Sci.*, vol. 301, pp. 264–272, 2014.
[90] K. Alexandrou *et al.*, "Improving the radiation hardness of graphene field effect transistors," *Appl. Phys. Lett.*, vol. 109, no. 15, 2016.
[91] S. Jain, A. Gupta, V. Shinde, V. R. Rao, and A. Gajarushi, "Application of mono layered graphene field effect transistors for gamma radiation detection," *2018 IEEE 13th Nanotechnol. Mater. Devices Conf. NMDC 2018*, no. 3, pp. 1–4, 2019.
[92] E. Cazalas, M. R. Hogsed, S. Vangala, M. R. Snure, and J. W. McClory, "Gamma-ray radiation effects in graphene-based transistors with h-BN nanometer film substrates," *Appl. Phys. Lett.*, vol. 115, no. 22, 2019.

[93] M. Schmitz *et al.*, "Fractional quantum Hall effect in CVD-grown graphene OPEN ACCESS," 2020.
[94] K. Dwlrq, R. I. Rz, R. Iru, W. K. Mqx, and H. G. X. Fq, "3Uhsdudwlrq Dqg &Kdudfwhul]Dwlrq Ri /Rz 7Hpshudwxuh &Xulqj &Rqgxfwlyh 6Loyhu 3Dvwh Iru 6Fuhhq 3Ulqwlqj," no. Msms, pp. 1–5, 2018.
[95] A. C. Ferrari and D. M. Basko, "Raman spectroscopy as a versatile tool for studying the properties of graphene," *Nat. Nanotechnol.*, vol. 8, no. 4, pp. 235–246, 2013.
[96] O. Frank, J. Vejpravova, V. Holy, L. Kavan, and M. Kalbac, "Interaction between graphene and copper substrate: The role of lattice orientation," *Carbon N. Y.*, vol. 68, pp. 440–451, 2014.
[97] I. Shlimak, A. Butenko, E. Kogan, and M. Kaveh, "Irradiation-induced broadening of the Raman spectra in monolayer graphene," *J. Appl. Phys.*, vol. 126, no. 19, 2019.
[98] M. Serry and M. A. Sakr, "Graphene-metal-semiconductor composite structure for multimodal energy conversion," *Sensors Actuators, A Phys.*, vol. 245, pp. 169–179, 2016.
[99] M. Serry, A. Sharaf, A. Emira, A. Abdul-Wahed, and A. Gamal, "Nanostructured graphene-Schottky junction low-bias radiation sensors," *Sensors Actuators, A Phys.*, vol. 232, pp. 329–340, 2015.
[100] M. A. Sakr, K. Elgammal, and A. Delin, "Performance-Enhanced Non-Enzymatic Glucose Sensor Based on Graphene-Heterostructure Mahmoud," *Sensors (Switzerland)*, vol. 20(1), pp. 1–15, 2020.
[101] Tawfik, M. W., Sharaf, A., & Serry, M. (2022). Monolayer Graphene Radiation Sensor with Backend RF Ring Oscillator Transducer. *Nanomaterials*, *12*(3), 305.
[102] Tawfik, M. W., Sharaf, A., & Serry, M. (2021, June). RF Ring Oscillator Graphene-Based Strain Sensor. In *2021 21st International Conference on Solid-State Sensors, Actuators and Microsystems (Transducers)* (pp. 1359-1362). IEEE.